Geochronology and Petrogenesis of the Early Silurian Zeluo Mafic-Ultramafic Intrusion, Eastern Tibet: Implications for the Tectonic Setting and Evolution of the Eastern Proto-Tethys Ocean

Hang Zhou[1], Wenxiao Zhou[1,2*], Ernest Chi Fru[2], Thomas C. Sheldrick[3], Haiquan Li[1], Bo Huang[4,5], Dong Fu[5], Yadong Xu[6]

[1]*Institute of Geological Survey, China University of Geosciences, Wuhan 430074, China*

[2]*School of Earth and Ocean Sciences, Centre for Geobiology and Geochemistry, Cardiff University, Cardiff CF10 3AT, Wales, the United Kingdom*

[3]*School of Geography, Geology and the Environment, University of Leicester, University Road, Leicester LE1 7RH, the United Kingdom*

[4]*National Observation and Research Station for Geohazards, Three Gorges Research Center for Geohazards, China University of Geosciences, Wuhan 430074, China*

[5]*Center for Global Tectonics, State Key Laboratory of Geological Processes and Mineral Resources, China University of Geosciences, Wuhan 430074, China*

[6]*School of Earth Sciences, China University of Geosciences (Wuhan), Wuhan 430074, China*

[*] Corresponding author: Wenxiao Zhou (zhouwenxiao@cug.edu.cn)

ORCID: https://orcid.org/0000-0003-4890-8803

Abstract Text: The Tibetan Plateau is a key region to understand the evolution of the Tethys Oceans. To better constrain the tectonic evolution of the Proto-Tethys Ocean on the western margin of the Yangtze plate, we present an integrated petrography, geochemistry, and zircon U-Pb-Lu-Hf isotope study on newly recognized early Silurian gabbro and serpentinite rocks from the eastern Yidun terrane of the Tibetan Plateau. Zircon U-Pb dating of the gabbro yields an Early Silurian age of 438.2 ± 2.8 Ma. Zircon $\varepsilon_{Hf}(t)$ values of 5.4 to 8.5 suggest a single-stage model age (T_{DM1}) ranging from 729 to 858 Ma. The gabbros exhibit low total rare earth element abundances but are moderately enriched in the light rare earth elements and the large-ion lithophile elements (e.g., Rb, Ba, and Sr), and display representative negative high-field strength elemental anomalies for Nb, Ta, Zr, and Hf on spidergrams. The gabbro and serpentinites were derived from a depleted mantle-like source made of garnet-spinel lherzolite composition, from a sub-arc mantle wedge that was metasomatized by slab dehydration. Thus, the gabbro and serpentinites record an Early Silurian subduction event of the Proto-Tethys Ocean under the Yangtze plate. Furthermore, this study confirms that the Yidun terrane on the western margin of the Yangtze plate is underlined by a Precambrian crystalline basement.

Keywords: Zircon U-Pb dating; Hf isotopes; Petrogenesis; Zeluo mafic-ultramafic rocks; Proto-Tethys Ocean

1. Introduction

Tethys, also known as the Tethys Sea or Tethys Ocean, was proposed in 1893 by the Austrian geologist Eduard Suess (Sengör, 1984), as a vast Mesozoic paleo-ocean that separated the Gondwana continent in the south, from the Angolan paleo-continent in the north. Much research has been devoted to geological studies of the East Tethys tectonic belt, mainly on the Tibetan Plateau, due to the importance of this extensive tectonic belt for understanding past plate reconstructions and geodynamics (Reid et al., 2005; Yan et al., 2005; Jian et al., 2008; Hu et al., 2009; Jian et al., 2009a; b; Roger et al., 2010; Wang et al., 2012; Zi et al., 2012; Hu et al., 2013; Hu et al., 2014; Wang et al., 2016a; Li et al., 2017; Zhao et al., 2017; Zhao et al., 2018; Liu et al., 2019; Xu et al., 2021). Based on a multidisciplinary dataset, four Tethyan ocean basins have been recognised in Asia (Metcalfe, 2021), the Proto-Tethys (Sinian-Silurian), Paleo-Tethys (Middle Devonian-Late Triassic), Meso-Tethys (Middle Permian-Late Cretaceous) and the Ceno-Tethys (Late Middle Triassic-Eocene).

The Sanjiang orogenic belt in southwest China has a complex geological architecture, being the result of intensive interactions between the Tethys Ocean, the Pan-Cathaysian terrain group and the Gondwana continental margin, and is formed by amalgamation of small continental blocks and arc terranes as a result of oceanic subduction (Jian et al., 2008; Jian et al., 2009a; b; Pan et al., 2016; 2020; Wang et al., 2021). The amalgamation of island arcs and oceanic basins with multiple small terranes, makes it difficult to determine the polarity of paleo-oceanic plate subduction in this orogenic belt. For example, previous studies have shown that the subduction polarity of the Proto-Tethys Ocean only involved southward subduction (Li et al., 2016a; b). However, recent research indicates that there was actually a complex subduction polarity during the Early Paleozoic, in the East Gondwana region (Liu et al., 2021). Although the Meso-Neotethyan domain in southern Tibet has been well studied, previous studies on the Tibetan Proto-Tethys have mainly focused on the Longmucuo-Shuanghu and the Changning-Menglian suture zones (Figure 1)–referred to collectively as the Longmucuo-Shuanghu-Changning-Menglian suture zones (Li et al., 2008; Wang et al., 2008; Jian et al., 2009b; Zhai et al., 2010; Mao et al., 2012; Zi et al., 2012; Wang et al., 2013; Zhai et al., 2013; Hu et al., 2014; Zhai et al., 2016; Wang et al., 2019a; Wang et al., 2020a; Wang et al., 2020b; Liu et al., 2021). More specifically, the lack of research on pre-Mesozoic igneous rocks from the Yidun terrane raises questions regarding the existence or absence of a Precambrian basement, and the overall tectonic evolution of the Proto-Tethys Ocean in the region.

This study explores the geological, geochemical, and geochronological significance of mafic-ultramafic rocks from Zeluo, Litang County, on the eastern edge of the Yidun terrane. We investigate their petrogenesis, tectonics and formation ages of the mafic-ultramafic rocks, and provide new constraints on the tectonic evolution and subduction polarity of the Proto-Tethys Ocean in the Sanjiang orogenic belt.

2. Geological setting

The Tibetan Plateau, composed of several micro-continental blocks, is an essential part of the Himalayan-Tethys tectonic domain (Zhao et al., 2020). From south to north

(Figure 1), the Himalayan, Lhasa, Qiangtang, Songpan-Garze, and East Kunlun blocks constitute the central tectonic units of the Tibetan Plateau (Dewey et al., 1988; Zhu et al., 2013). These blocks assembled after the closure of the Proto-Tethys, the paleo-Tethys, and the neo-Tethys sutures (Pan et al., 2012; Zhao et al., 2018; Xu et al., 2021). This study concentrates on the Garze Tibetan Autonomous Prefecture, close to the Garze-Litang suture zone, Sichuan Province (Figure 2), and is divided into the Yidun and Zhongza-Zhongdian terranes, based on stratigraphic differences (Reid et al., 2005). The Zhongza-Zhongdian terrane consists mainly of Paleozoic clastic and weakly metamorphosed carbonate lithologies, accompanied by a small amount of Neoproterozoic granitic gneisses and metamorphosed volcanic rocks (Xu et al., 2021).

In contrast, the Yidun terrane is more complex, consisting largely of Triassic volcano-sedimentary rocks and Late Triassic granitic-type lithologies (Figure 2). However, Early Paleozoic sequences were identified in the eastern part of the Yidun terrane (i.e., O_1t, Figure 3). The results of detrital zircon U-Pb radiometric dating and sediment source analysis indicates that the Yidun terrane was a part of the Yangtze plate in the Early Paleozoic, before being rifted apart during the Late Paleozoic (Xu et al., 2021). The Triassic volcano-sedimentary rocks are primarily divided into the Tumugou and Lamaya Formations (Figure 3). The Tumugou Formation is composed of andesite, tuff, and clastic sandstones, while the Lamaya Formation consists of epizonal metamorphic sandstone and slate which have a conformable contact with each other. The Tumugou and Lamaya Formations were deposited 225–216 Ma and were derived from the Qiangtang and Zhongza-Zhongdian terranes (Xu et al., 2021). The Zeluo ultramafic-mafic rocks are the focus of this study and have a fault-controlled contact with the Tumugou Formation and Triassic granite (Figure 3).

3. Petrographic characterization

All samples were collected from Zeluo village, Litang County, on the eastern margin of the Yidun terrane. Field photographs and sample microphotographs are shown in Figure 4 and Figure 5, respectively. Twenty-five zircon crystals were obtained from a mafic intrusive rock sample (TW5546) for zircon U-Pb geochronology. Sixteen mafic, and three ultramafic rocks, were sampled for whole-rock geochemical analysis.

The ultramafic rocks consist of partially serpentinized peridotites, made up primarily of harzburgite and strongly serpentinized dunites. The peridotite samples show various degrees of serpentinization (Figure 4a-c), while the heavily serpentinized dunites, which contain small amounts of olivine crystals and magnesiochromite (Figure 5e, f), occur as lenses or patches in the Zeluo gabbro (Figure 4a-c). In some of the dunite samples, the magnesiochromite is altered to magnetite (Figure 5e, f).

The metamorphosed gabbro is composed mainly of tabular, subhedral to prismatic plagioclase and subhedral granular pyroxene crystals (Figure 5d). Most of the plagioclase crystals have been replaced and altered to zoisite, albite and sericite. In addition, the majority of altered actinolite and biotite crystals are subhedral with a granular texture. Based on pseudo crystal shape, it is speculated that the altered crystals were originally pyroxenes, with minor quantities of amphibole crystals having also been replaced.

4. Analytical Methods

4.1. LA-ICP-MS U-Pb isotopes

Zircon crystals from one fresh sample (TW5546) were separated by using standard heavy liquid and magnetic techniques. Representative crystals were selected under a binocular microscope, set in a resin mount, and polished until their centers were exposed. Cathodoluminescence (CL) images of the zircon crystals were obtained to observe their internal textures and help select appropriate analytical sites. Zircon U-Pb dating was conducted using a laser ablation inductively-coupled plasma mass spectrometer (LA-ICP-MS) at the State Key Laboratory of Geological Processes and Mineral Resources (GPMR), China University of Geosciences (Wuhan). A GeoLas 2005 platform and an Agilent 7500a ICP-MS instrument was used to sample and acquire the ion-signal intensities. The detailed analytical techniques and data processing procedures were as described by Liu et al. (2009); Liu et al. (2008);Liu et al. (2010). A common Pb correction method was applied as described by Andersen (2002). The U-Pb ages were calculated and plotted using the ISOPLOT software (Ludwig, 2003).

4.2. LA-MC-ICP-MS Lu-Hf isotopes

In situ Lu-Hf isotope analysis was conducted using a Neptune Plus MC-ICP-MS (Thermo Fisher Scientific, Germany) in combination with a Geolas HD excimer ArF laser ablation system (Coherent, Göttingen, Germany) at GPMR. A “wire” signal smoothing device was included in this laser ablation system, to enable the production of a smooth signal (Hu et al., 2015). Helium was used as carrier gas within the ablation cell and was merged with argon after exiting the ablation cell. Small amounts of nitrogen were added to the argon gas flow to enhance signal sensitivity (Hu et al., 2012). All data acquired on the zircon crystals was done by using a single spot ablation technique, with a spot size of 44 μm. The energy density used in this study was ~7.0 J cm^{-2}. Each measurement consisted of 20s of acquisition of the background signal followed by 50s of ablation signal acquisition. The operating conditions for the laser ablation system and the MC-ICP-MS instrument, and analytical methodology, were as described by Hu et al. (2012). The $^{179}Hf/^{177}Hf$ and $^{173}Yb/^{171}Yb$ ratios were used to calculate the mass bias of Hf (βHf) and Yb (βYb), normalized to $^{179}Hf/^{177}Hf = 0.7325$ and $^{173}Yb/^{171}Yb = 1.132685$ (Fisher et al., 2014) using an exponential correction for mass bias. Interference of ^{176}Yb on ^{176}Hf was corrected by measuring the interference-free ^{173}Yb isotope and using $^{176}Yb/^{173}Yb = 0.79639$ (Fisher et al., 2014) to calculate $^{176}Yb/^{177}Hf$. Similarly, the relatively minor interference of ^{176}Lu on ^{176}Hf was corrected by measuring the intensity of the interference-free ^{175}Lu isotope and using the recommended $^{176}Lu/^{175}Lu = 0.02655$ (Fisher et al., 2014) to calculate $^{176}Lu/^{177}Hf$. We used the mass bias of Yb (βYb) to calculate the mass fractionation of Lu because of their similar physicochemical properties. Off-line selection and integration of analyte signals, and mass bias calibrations were performed using ICPMSDataCal (Liu et al., 2010).

During the LA-MC-ICP-MS analysis, three standard zircons, 91500, GJ-1 and

Temora-2 were used. Zircon 91500 was utilised as the external standard, whereas GJ-1 and Temora-2 were treated as unknown samples to verify the accuracy of the calibration method. Measured $^{176}Hf/^{177}Hf$ ratios of standard zircons 91500, GJ-1 and Temora-2 were 0.282308 ± 0.000019 (2σ, n = 36), 0.282011 ± 0.000021 (2σ, n = 16) and 0.282671 ± 0.000034 (2σ, n = 16), respectively, which are consistent with their recommended values of 0.282305 ± 6, 0.282000 ± 5, and 0.282686 ± 8 (2σ) (Fisher et al., 2014).

4.3. Whole-rock geochemistry

Preliminarily processing of fresh samples was carried out at the Geological Survey Institute, China University of Geosciences, Wuhan. Samples were powdered to grain size of less than 75 μm at the State Key Laboratory of Biogeology and Environmental Geology, China University of Geosciences, Wuhan. Care was taken during the preparation of the powder to eliminate possible contamination. Major and trace element analyses were carried out at ALS Minerals–ALS Chemex, Guangzhou, China. Whole-rock major element concentrations were determined by initial acid digestion in lithium borate, followed by X-ray fluorescence (ME-XRF26d) analysis, with errors being less than 1%. Trace element and rare earth element concentrations were determined by mixed acid digestion and plasma mass spectrometry (M61-MS81). Most of the illustrations in this paper were produced using GEOKIT software (Lu, 2004).

4.4. Mineral chemistry

Mineral chemical compositions for olivine and clinopyroxene were obtained at the

Center for Global Tectonics, School of Earth Sciences, China University of Geosciences, Wuhan, using a JEOL JXA-8230 electron microprobe with an acceleration voltage and beam current of 5 kv and 20 nA, respectively. An analytical beam diameter of 3 μm and background counting time of 5s was implemented. Elemental calibration standards set according to procedures outlined in Wang et al. (2019b), produced analytical errors of generally less than 2%.

5. Results

5.1. Zircon U-Pb geochronology

The zircon LA-ICP-MS U-Pb analytical results are given in Table S1 and Figure 6. Analyzed zircons were euhedral to subhedral, being mostly rhombic, prismatic, or short columnar in shape. A few were irregular or broken ~120–200 μm long crystals with an aspect ratio of ~1.5–3. Their Th and U contents range from 158–883 ppm and 236–603 ppm, respectively, with generally high Th/U ratios of 0.67–1.55 (Table S1). Cathodoluminescence (CL) imaging revealed that the 25 analyzed zircon crystals were non-metamorphic, possessing typical ring structures apparently of igneous origin (Figure 6a). The $^{206}Pb/^{238}U$–$^{207}Pb/^{235}U$ associated ages of 23 zircons ranged from 410 to 445 Ma, with a weighted average $^{206}U/^{238}Pb$ age of 438.2 ± 2.8 Ma and a greater than 95% data concordance (Figure 6b). Zircon test on crystal No.6 and No.16 were discarded because they yielded a younger and older age corresponding to a poor concordance of 92% and 95%, respectively, with large analytical errors (Figure 6a).

5.2. Mineral chemistry

The major element content and geochemical parameters calculated by Geokit Geochemistry (Lu, 2004), of olivine and pyroxene crystals from the Zeluo mafic-ultramafic samples are listed in Table S2 and Table S3, respectively.

5.2.1. Olivine

Olivine crystals in the Zeluo ultramafic rocks occur as fine-grained 10–50μm aggregates (Figure 5e, f). They are characterized by high Fo values, calculated as Fo = (100 × Mg)/(Mg + Fe) in moles, spanning 92.64–93.54, a MnO content of 0.28–0.39 wt.%, NiO concentrations down to 0.101 wt.%, and widely varying low CaO values of 0.03–0.22 wt.%.

5.2.2. Pyroxene

The pyroxene crystals are characterized by relatively high MgO (16.04–93.54 wt.%), CaO (25.66–26.1 wt.%), and FeO (1.13–2.8 wt.%). The En values range from 44.41–46.47 and Fs from 3.19–4.3, indicating that they are of diopside composition (Morimoto, 1988). The cation number for the pyroxenes were calculated based on 6 oxygen atoms and 4 cations.

5.3. Bulk-rock geochemical compositions

5.3.1. Major elements

The major and trace element concentration data obtained from this study are displayed in Table S4. For the ultramafic samples loss-on-ignition (LOI) values range from 7.94 to 8.37 wt.%, with an average of 8.11 wt.%. They contain 35.37–36.72 wt.% SiO_2 with an estimated average of 36.23 wt.%. Measured MgO content was high and range from 27.7–30.4 wt.%, while the TFe_2O_3 composition span 13.64–15.61 wt.%, being generally low in TiO_2 (0.45–0.53 wt.%) and total alkali (K_2O+Na_2O) (0.01–0.12 wt.%) contents. These ultramafic rocks record an associated Al_2O_3 and CaO concentration of 4.66–4.88 wt.% and 5.25–7.08 wt.%, respectively.

Comparatively, LOI values for the mafic samples change from 0.85 to 2.74 wt.%, averaging 1.65 wt.%. They contain up to 43.14–50.59 wt.% SiO_2 that average 46.65 wt.%. They record a high MgO content of up to 6.98–17.65 wt.%, 6.79–15.94 wt.% TFe_2O_3, 0.45–2.45 wt.% TiO_2, and a total alkali concentration of 1.17–5.48 wt.%. The tholeiitic mafic rocks (Figure 7a) with up to 8.11–14 wt.% CaO concentrations, were found to be relatively enriched in TiO_2 and alkali metals compared to the ultramafic rocks.

5.3.2. Trace element variations

The ultramafic rocks display REE chondritic distribution patterns (Figure 7b) that are characterized by decreasing enrichment from left to right. The sloping down REE pattern exhibits negative Eu anomalies (δEu = 0.66–0.71) and on a primitive mantle plot, the rocks are shown to be depleted in large-ion lithophile elements (LILEs) such as Rb, Ba, and Sr, but relatively enriched in Nb, Ta, Zr, and HF compared to neighboring elements (Figure 7c). Compared to typical OIB and MORB, the ultramafic rocks are more depleted in the HREEs.

To the contrary, the mafic rocks tend to possess slightly positive Eu anomalies (δEu = 1.04–1.41) and an average δEu of 1.18 (Figure 7b). Their REE chondritic distribution reveals a smooth curve with a tendency to decline to the right. They are characterized by LREE/HREE ratios of 2.75–5.30 (Avg = 3.44) and an E-MORB-like $La/Yb_{(N)}$ range of 2.42–6.78. The LILEs Rb, Ba, Pb, and Sr are enriched on the primitive mantle plot, while the HFSEs Nb, Ta, Zr, and Hf are depleted (Figure 7c). Collectively these observations suggest a predominantly arc-like geochemical signature (Zhao and Zhou, 2007).

5.4. Lu-Hf isotope distribution

Spot analyses on 23 zircon crystals purified from the gabbro yielded Lu/Hf values ranging from -0.91 to -0.95 (Table S5). These values are much lower than the average values of -0.34 and -0.72 observed for the mafic and siliceous crusts, respectively (Vervoort and Jonathan Patchett, 1996; Amelin et al., 1999). The gabbroic $^{176}Hf/^{177}Hf$ zircon grain ratios vary from 0.282679 to 0.282760 and correspond to $\varepsilon_{Hf}(t)$ values of 5.3–8.5 with a mean of 6.7 (Figure 8a). This points to single-stage Hf model ages (T_{DM1}) of 858–729 Ma with a mean of 802 Ma for when the gabbro formed.

6. Discussion

6.1. Timing of Early Paleozoic mafic-ultramafic magmatism at Zeluo

Based on data compiled from Western Australia, zircons of igneous origin rarely possess Th/U values <0.1, while metamorphic zircons encompass values ranging from <0.01 to >10 (Yakymchuk et al., 2018). However, it has been proposed that a Th/U ratio of <0.4 is generally a good first-order indicator for distinguishing recycled metamorphic zircons from igneous lithologies (Yakymchuk et al., 2018). This is because Th^{4+} has a larger ionic radius than U^{4+}, and therefore exhibits a weaker stability than U in the zircon crystal lattice. As a result, Th^{4+} is easier to expel from the zircon crystal than U^{4+} during metamorphic recrystallization, lowering the Th/U ratio in recycled metamorphic zircons (Hoskin and Black, 2000). Twenty-three of the 25 analyzed zircon crystals exhibit high Th/U ratios ＞0.4 and ranging from 0.67–1.55 (Table S1), pointing to an igneous origin. Moreover, cathodoluminescence images show that these zircon crystals possess ring structures typical of an igneous source and lack any evidence for metamorphic recrystallization. The zircon crystals clustered at ~438 Ma, about 200 Ma older than the ~237–216 Ma Triassic magmatism previously recorded from the region (Figure 3) (Fang et al., 2017). Therefore, an Early Silurian age of ~438 Ma is taken as the most parsimonious crystallization age of the gabbro.

Early Paleozoic ultramafic-mafic rocks, including ophiolites and arc igneous rocks (Figure 1) are also present in the Longmucuo-Shuanghu-Changning-Menglian suture in the Tibetan Plateau, China. For example, U-Pb ages of 438 ± 11 Ma and 431.7 ± 6.9 Ma have been reported by two independent studies on zircons retrieved from a gabbro pile in the western section of Guoganjianian, south Qiangtang (Li et al., 2008; Wang et al., 2008). Furthermore, zircon U-Pb ages of ~437–429 Ma for arc igneous rocks in the same suture zone have also been reported (Liu et al., 2021). Another example of middle–late Silurian intermediate-mafic magmatism was located just south of the Changning-Menglian suture zone, at 421.2 ± 1.2 Ma (Mao et al., 2012). These ages coincide with the ~450 to 400 Ma late-stage evolution of the Proto-Tethys oceanic basin (Li et al., 2016b; Wu et al., 2020). Collectively, the data (Figure 1) show that the Proto-Tethys Ocean, in the Tibetan Plateau, underwent continuous evolution during the Early Paleozoic, and that the Zeluo mafic-ultramafic rocks represent a likely final phase of the Early Paleozoic magmatism.

6.2. Alteration

The influence of alteration and metamorphism needs to be evaluated before pursuing any discussion on source characteristics and tectonic setting (Polat et al., 2002; Polat and Hofmann, 2003). Previous studies have shown that the LOI value can be used as a proxy of hydrothermal alteration and that the reconstructed chemical composition of pristine basaltic melts are reliable when LOI values are <2% (Rosenstengel and Hartmann, 2012; Hartmann et al., 2015). In this regard, the 0.85–2.74 wt.% LOI values for the mafic rocks imply weak alteration, while the higher 7.94–8.37 wt.% concentrations for the ultramafic rocks indicate more extensive alteration (Table S4). To assess whether highly susceptible elements such as K or Rb, have been altered we utilize a K_2O vs. Rb plot (Figure S1a). This is because K and Rb have opposite alteration trends, whereby K content decreases at the expense of significant Rb increase during alteration (Hartmann et al., 2015). The constant K_2O vs. Rb slope, together with the strong positive correlation recorded for the mafic samples are consistent with minimal alteration, while the ultramafic sample suite is harder to assess due to the lack of sufficient data spread.

HFSEs (e.g., Zr, Th, Ta, and Nb, etc.) are geochemically stable and resistant to metamorphism, alteration, and weathering (Pearce and Cann, 1973; Winchester and Floyd, 1977). The Zr and Hf concentrations in the Zeluo pluton are seen to progressively decrease proportionally (Figure S1b), likely related to the crystallization properties of heavy minerals such as zircon. In reality, a near-constant Zr/Hf ratio has been observed in many magmatic suites, including low to moderate metamorphic magmas (Dostal and Chatterjee, 1995; Bryant et al., 1997; Zhang et al., 2014; Wu et al., 2016b), while the Zr/Hf ratio of most crustal rocks is close to 37 (Brooks, 1970). However, in some cases, these elements are actually mobile and can be transported by magmatic-, metamorphic-, and submarine-hydrothermal solutions (Jiang et al., 2005). Studies show that Zr and Hf have obvious differentiation in fluorine-rich fluids or highly evolved hydrothermal fluids, where the activity of Hf is higher than that of Zr, resulting in a very low Zr/Hf ratio of ~1–2 in the host rock or heavy minerals (Jiang et al., 2005; Wang et al., 2010). On a Zr vs. Hf, and a Ta vs. Nb diagram (Figure S1b, c), there is a strong linear relationship for both the ultramafic and mafic rock samples. Therefore, the HFSEs in the Zeluo samples were likely resistant to change from any alteration processes that occurred.

In summary, the constant K_2O/Rb ratio, low LOI and high alkali content of the mafic rocks indicate insignificant modification by alterative processes, while the ultramafic rocks have undergone more significant alteration.

6.3. Crustal contamination

The process of crustal contamination can change a magmas composition and thermal properties. However, if a magma ascends quickly through the lithosphere or crust, it may avoid significant contamination (O'Hara, 1968).

A combination of Ce/Pb and La/Nb values can be used to assess the degree of crustal contamination and mantle mixing processes (e.g., Barry et al. (2003); Rooney et al. (2007); Sheldrick et al. (2018)), and basalts with high Ce/Pb ratios in the range of ~20–30, are unlikely to have assimilated crustal material (Rooney et al., 2007). La/Nb ratios of 0.81–1.9 and Ce/Pb ratios of 0.38–3.3 for our samples, plot in the crust-mantle mixing region on a La/Nb-Ce/Pb diagram (Figure 9a). However, previous work has shown that Pb is preferentially incorporated into fluids produced by slab dehydration (Gill and Condomines, 1992; Johnson and Plank, 2000). Therefore, Pb concentrations in a source region can be enriched by metasomatism following slab dehydration, resulting in melts from the metasomatised source possessing low Ce/Pb ratios. Furthermore, when we consider that many crustal components are enriched in Th and Pb (Zhao and Zhou, 2007), the low Th, Th/Yb, and high Nb/Th in the mafic and ultramafic rocks indicate that crustal contamination was likely small (Figure 9b, c). Thus, the extremely low Th content of the mafic rocks is uncharacteristic for significant crustal contamination. The contribution of crustal materials in the generation of high Pb concentrations in the mafic rocks is therefore considered to be insignificant. Crustal xenoliths are absent from both the ultramafic and mafic rocks, which together with the lack of evidence for inherited zircon crystals, further supports minimal crustal contamination.

Overall, although it seems unlikely that the ultramafic and mafic magmatism could have moved through the continental crust without undergoing crustal contamination, based on the results discussed above, crustal contamination was broadly minimal.

6.4. Nature of the mantle source region

The presence of oscillatory zoning in the zircon crystals indicate that they have not been significantly modified by metamorphic processes and therefore likely retain their original geochemical composition. Zircon $^{176}Hf/^{177}Hf$ ratios are believed to represent the Hf composition of a magmatic system, at the time of their crystallization (Wu et al., 2007). Many scientists attribute low $\varepsilon_{Hf}(t)$ values of <0 to an ancient crustal source (e.g., Iizuka et al. (2009)). Alternatively, $\varepsilon_{Hf}(t)$ values >0 may indicate a depleted mantle magma source (e.g., Amelin et al. (2000)).

As a corollary, the varying zircon $\varepsilon_{Hf}(t)$ values of 5.3–8.5 for the Zeluo mafic rocks (Figure 8a), imply a depleted mantle source for the magma. However, if we consider what the theoretical $\varepsilon_{Hf}(t)$ values for depleted mantle should be at ~438 Ma when the mafic magmatism occurred, the values should be closer to ~15 (Figure 8b). The Zeluo mafic rocks have an $\varepsilon_{Hf}(t)$ signature lower than expected for a melt extracted from an isolated and depleted mantle source. These positive $\varepsilon_{Hf}(t)$ values are comparable to zircons from a mid-Ordovician metamorphic gabbro in the Longmucuo-Shuanghu suture zone in northern Tibet, with $\varepsilon_{Hf}(t)$ = 4.5–5.9 (Zhai et al. (2010)), or to the Dongzhulin layered gabbro with $\varepsilon_{Hf}(t)$ = 10.3–12.6 in the Devonian, Jinshajiang suture zone (Wang et al. (2012); Figure 1 and Figure 8b), which confirms the existence of a depleted mantle beneath the crust in the studies area during the early Paleozoic. If the zircon Hf isotope two-stage crust model ages (TDM) are older than their formation ages, it can be concluded that the magma was contaminated by crustal materials (Wu et al., 2007; Su et al., 2011), implying the calculated model ages may represent an average age of the contamination source (Arndt and Goldstein, 1987; Ortega-Obregón et al., 2014). In other words, TDM provides age information for crust contamination (Liu et al., 2016b). The Zircon Hf model ages of T_{DM1} = 729–858, T_{DM2} = 972–1132 for the Zeluo mafic rocks are much older than their formation ages. Such an observation indicates that crustal material was incorporated into the depleted mantle prior to mafic melt extraction. This raises questions as to how and where Neoproterozoic strata were added to the Early Silurian mafic-ultramafic system. Previous studies indicate that Neoproterozoic sequences may exist in Yidun terrane (Wu et al., 2016a; Tian et al., 2020; 2022). Thus, the mafic rocks may have acquired their depleted mantle-like $\varepsilon_{Hf}(t)$ signature from subducted Proto-Tethys oceanic crust components or the Neoproterozoic strata of the Yidun terrane being melted and incorporated into the source region. The mafic rocks are enriched in the LILEs and LREEs, and relatively depleted in the HFSEs and HREEs (Figure 7b, c). The simplest explanation for the enrichment and depletion of these different trace element systems would be to invoke a source which had undergone fluid metasomatism from the subduction of oceanic crust (Pearce, 1982). During fluid processes, Th is an immobile element compared to Ba and Pb (Gill and Condomines, 1992; Johnson and Plank, 2000), but is efficiently transferred from the slab in sediment melt (Johnson and Plank, 2000). Fluids derived from dehydration reactions, from subducted pelagic sediments, are expected to have a high Ba/Th and Ba/La ratios, but low $(La/Sm)_N$ and Th/Yb ratios (e.g., Woodhead et al. (2001) and Elliott (2003), Figure 10a, b). Such a source seems possible when we consider that the Zeluo mafic-ultramafic rocks are located on the western margin of the Yangtze plate, which is adjacent to the Proto-Paleo-Tethys suture. Such fluids would enrich the mantle in Pb through metasomatism, consistent with the results observed in Figure 7c. In addition, previous work which studied the subduction of Proto-Tethys oceanic crust (Figure 1) details magmatism with similar geochemical signatures near adjacent regions (Figure 7b and Figure 10a, b). Overall, the data suggest that the source region was probably a sub-arc mantle wedge, which was metasomatized by fluids extracted from the Proto-Tethys subducting slab.

6.5. High Fo olivine values

Previous studies have shown that olivine in peridotite of typical Archean lithospheric mantle has high Fo values ~92 (Boyd, 1989). For example, elevated olivine Fo values of ~92 in Hebi high-$Mg^{\#}$ peridotite and Siziwangqi peridotite xenoliths were considered as residues of the Archean lithospheric mantle (Zheng et al., 2001; Tang et al., 2013; Zhang et al., 2021). In addition, the CaO content of <0.1 wt.% is another significant feature of Archean mantle-derived olivine (Simkin and Smith, 1970; Xu et al., 2010; Prelević et al., 2013). On the other hand, olivine crystallized from melts tend to have >0.1 wt% CaO concentrations and higher MnO contents compared to the mantle or lithospheric xenocrysts (Tang et al., 2004; Kamenetsky et al., 2006; Guo et al., 2015; Cheng and Guo, 2017). In this study, the high CaO concentration in the analyzed olivine opposes an Archean mantle residue source for the Zeluo ultramafic rocks, likely indicating that the olivine crystals are a product of fractional crystallization in the melt. Harker diagrams (Figure 11a-c) show a positive relationship between MgO versus Cr_2O_3, TFe_2O_3, and NiO for the mafic-ultramafic samples, reflecting potential fractionation of olivine, pyroxene, and accessory minerals (e.g., chromite). Compared with Fe, Mg in a magma is easily captured and incorporated by early fractional olivine crystallization. Therefore, the slope of Mg/Fe ratios can be expected to increase gradually during magma evolution and differentiation (Figure 11b), which supports olivine crystallization from the melt. In addition, SiO_2 correlates with Al_2O_3, TFe_2O_3, and MgO (Figure 11d-f), further indicating that fractional crystallization of pyroxene, amphibole and plagioclase played a key role in the evolution of the mafic-ultramafic suite (Meng et al., 2020).

During the crystallization of primitive magma, the exchange of Fe and Mg between olivine and melt follows a certain partition coefficient, defined by $K_D = (FeO/MgO)_{Ol}/(FeO/MgO)_{melt} = 0.3 \pm 0.03$ (Roeder and Emslie, 1970). Therefore, the Fo value and molar MgO/FeO ratios in primary olivine are often used to estimate the composition of primitive magma (e.g., Chai and Naldrett (1992); Sun et al. (2009); Jia et al. (2018)). It is worth noting that when using olivine to estimate the composition of parent magma, two preconditions need to be met: (1) olivine is the only or main cumulate phase in the rock and (2) ultramafic rocks have a small LOI (Bao et al., 2020).

In this study, ultramafic rocks have a high LOI and are rich in magnetite (Figure 5e, f), shown by recent studies to be a direct product of serpentinization (Maffione et al., 2014; Nutman et al., 2021). Thus, Zeluo ultramafic rocks experienced strong serpentinization, which might have resulted in variable Fo values in olivine (Nutman et al., 2021). During serpentinization, Fe-rich olivine is transformed into Fe-poor olivine, according to the following formula: Secondary-olivine (Fe-rich) + water = Secondary-olivine (Fe-poor) + SiO_2 (aq) + magnetite + H_2 (Dandar et al., 2019). Serpentinized olivine usually has high narrow-range distributed Fo values, i.e., $Fo_{max} - Fo_{min} < 2$ (e.g., Nutman et al. (2021) and Dandar et al. (2019)). On the contrary, the unaltered primitive olivine usually has a larger range of variable Fo values, because the Mg content in the magma gradually decreases with olivine crystallization (Sun et al., 2009).

In conclusion, olivine in this study has high and relatively concentrated Fo values and coexists with magnetite, indicative of strong secondary changes and therefore cannot be used to estimate the composition of the primitive magma, but $Mg^{\#}$ of the whole rock is less affected. To avoid the error caused by LOI, we have recalculated the Zeluo ultramafic-mafic rock MgO and TFe_2O_3 concentrations, with their total major element contents being 100 wt.%. This resulted in a $Mg^{\#}_{ultramafic}$ = 77.5–81.2 and averaging 79.3, and a $Mg^{\#}_{mafic}$ = 51.3–72.3, with an average of 63.1. Although the $Mg^{\#}$ of the samples fluctuated greatly due to magma differentiation, we agree that the $Mg^{\#}$ of the Zeluo ultramafic-mafic rocks conform to the $Mg^{\#}$ = 63–73 range of primitive mantle-derived magma (Green (1975)).

6.6. Partial melting of mantle peridotite

The typical Archean cratonic mantle is generally composed of harzburgites and cpx-poor lherzolites (Boyd, 1989). Generally, spanning the Archean to the Phanerozoic Eon, the lithospheric mantle changes from dominant harzburgites to being predominantly lherzolites (Tang et al., 2008). For mantle-derived rocks, REE abundances and ratios can be used to determine the composition of their source, and the degree of melting (Aldanmaz et al., 2000; Zhao and Zhou, 2007). It has been shown that Sm, La, and Yb have similar partition coefficients ($D_{spinel/melt}$) of ~0.01 in spinel (McKenzie and O'Nions, 1991). When spinel lherzolite undergoes partial melting, the mantle and extracted melt inherit similar Sm/Yb ratios (Aldanmaz et al., 2000) and a relatively flat melting trend on a Sm/Yb vs. Sm and La/Sm diagram. On the other hand, garnet has a high partition coefficient for Yb ($D_{garnet/melt}$) of ~4.03 relative to ~0.01 for Sm (McKenzie and O'Nions, 1991), in basaltic melts. The partial melting of garnet lherzolite, when garnet remains as a remnant mineral, produces a steeper melting trend than for spinel lherzolite (Figure 12a, b). The Zeluo mafic-ultramafic samples plot near the garnet-spinel lherzolite melting trend (Figure 12a, b). However, La/Sm ratios decrease with increasing degrees of partial melting (Aldanmaz et al., 2000), resulting in the mafic samples plotting towards a melting curve with a greater garnet control. Overall, this model indicates that the Zeluo mafic-ultramafic rocks may have crystallized from a melt produced by ~20% partial melting of garnet-spinel lherzolite (Figure 12a, b).

We have interpreted the Zeluo mafic-ultramafic intrusions on the western margin of the Yangtze plate as evidence for arc magmatism, with a source region that was modified by fluids derived from a subducted slab. But such an interpretation raises a question of whether the mantle relic was produced by older subduction events or whether magmatism coincided with an ongoing subduction event. Firstly, 439.3 ± 3.5 Ma continental flood basalts have been identified from the Jinshajiang suture zone on the western margin of the Yangtze plate, which are associated with an early continental rifting episode (Jian et al., 2009a; b). Secondly, a ~422 ± 6.1 Ma mafic rock block with OIB characteristics, from the Jinshajiang suture zone, was interpreted to have formed in a tectonic setting that was undergoing a subduction accretion (Liu et al., 2019). This suggests that the Jinshajiang paleo-Tethys was most likely produced in a back-arc basin, which was the result of the subduction of the Proto-Tethys ocean (Wang et al., 2012). The opening of the Jinshajiang-Ailaoshan paleo-Tethys also led to the separation of the Simao terrane from the Yangtze plate in the mid-late Paleozoic (Jian et al., 2009b). The combination of these observations leads us to believe that the Zeluo intrusions were in fact related to active subduction during the early Silurian.

6.7. Geodynamic implications for the East Proto-Tethys Ocean

In the Proto-Tethys oceanic domain there are many microcontinents/continents, including the Yangtze, Cathaysia, Tarim, Qaidam, Qilian, Indochina, north Qiangtang, and south Qiangtang blocks/micro-continental blocks which were distributed widely during the Early Paleozoic (Li et al., 2016b). Most of them were either located on the northern margin of the eastern Gondwana continent, amalgamated with the Gondwana continent, or dispersed amongst each other and the oceans (Figure 13a). A paleomagnetic study by Huang et al. (2018) concluded that the South China Plate maintained its relative position next to the western part of the Australian plate and the northern part of the Indian plate from the beginning of the Neoproterozoic, to the end of the Paleozoic (Figure 13a).

Studies on gabbro samples, from ophiolites, aged between 432–507 Ma from the Longmucuo-Shuanghu suture zone and Changning-Menglian suture zone, indicate that there was an ocean basin (Longmucuo-Shuanghu-Changning-Menglian Proto-Tethys Ocean, LSCMTO, Liu et al. (2021)) of uncertain size at the northern margin of the Cambrian-Silurian Gondwana continent (Li et al., 2008; Wang et al., 2008; Zhai et al., 2010; Wang et al., 2013; Hu et al., 2014; Liu et al., 2021). The LSCMTO (Figure 13a) may have separated the South China plate from the Gondwana continental region (Condon et al., 2005; Wu et al., 2020)

Magmatism derived from arc processes, when located on the edge of a tectonic plate, provides the best opportunity to determine the subduction polarity of a paleo-ocean. The discovery of the Zeluo early Silurian mafic-ultramafic rocks provide evidence for oceanic plate subduction, and therefore indicates that there was northwestward subduction along the western side of the Yangtze plate, of the LSCMTO (Figure 13b). On the other hand, a large number of 446–430 Ma magmatic rocks have also been identified from the south Qiangtang and Baoshan blocks (Zhao et al., 2016; Liu et al., 2021), which are considered to be the products of southeastward subduction of the LSCMTO oceanic plate in the Early Paleozoic (Wang et al., 2020b). Therefore, taken together, this information indicates bidirectional subduction of the LSCMTO oceanic crust, southeastward towards East Gondwana and northwestward towards Yangtze (Figure 13a, b).

Although the Zeluo mafic-ultramafic rocks are products of early Silurian magmatism on the western margin of the Yangtze plate, they were displaced by the NW-trending Litang active fault during the Holocene (Figure 2; Xu et al. (2005)). However, a study which looked at a combination of geophysical measurements, geomorphological features, and quaternary neo-tectonic plate movements, indicates that the displacement distance of individual blocks within the Litang Fracture Zone since the Holocene did not exceed 1 km (Xu et al., 2005). Therefore, the Zeluo mafic-ultramafic rocks are not products of an event from outside the Yidun terrane but rather are magmatic rocks which formed within it. These Paleozoic magmatic rocks record oceanic subduction and supports the idea of a Precambrian crystalline basement beneath the Late Triassic sediments in the Yidun terrane (He et al., 2013; Wu et al., 2016a), while others propose the Yidun terrane developed on an oceanic crust (e.g., Leng et al. (2014))

7. Conclusion

(1) The Zeluo mafic-ultramafic rocks formed during the Early Silurian, at 438.2 ± 2.8 Ma, by ~20% partial melting of a garnet-spinel lherzolite enriched mantle. The dehydration of subducting oceanic crust metasomatized the overlying mantle wedge source.

(2) Primitive mantle-derived magma from an ancient supra-subduction zone complex formed the mafic and the ultramafic magmas.

(3) The Longmucuo-Shuanghu-Changning-Menglian Proto-Tethys Ocean, located between Yangtze and East Gondwana, underwent bidirectional subduction in the Early Silurian. The Zeluo mafic-ultramafic rocks provide evidence for the northwestward subduction of this ocean.

(4) The laterally continuous early Silurian magmatic rocks found in the Yidun terrane confirm the existence of a Precambrian crystalline basement.

ACKNOWLEDGEMENTS

Professor Robert J. Stern and two anonymous reviewers were appreciated for their constructive comments and reviews, which substantially improved this work. Financial support for this study was jointly provided by the National Natural Science Foundation of China (Grant No. 41703024, 42102244, 42102268), the China Geological Survey Project (Grant No. DD20190811, DD20221814) and the China Scholarship Council (Grant No. 201906415032).

References

Aldanmaz, E., Pearce, J.A., Thirlwall, M.F., Mitchell, J.G., 2000. Petrogenetic evolution of late Cenozoic, post-collision volcanism in western Anatolia, Turkey. Journal of Volcanology and Geothermal Research, 102(1): 67–95.https://doi.org/10.1016/S0377-0273(00)00182-7

Amelin, Y., Lee, D.C., Halliday, A.N., 2000. Early-middle archaean crustal evolution deduced from Lu-Hf and U-Pb isotopic studies of single zircon grains. Geochimica et Cosmochimica Acta, 64(24): 4205–4225.https://doi.org/10.1016/S0016-7037(00)00493-2

Amelin, Y., Lee, D.C., Halliday, A.N., Pidgeon, R.T., 1999. Nature of the Earth's earliest crust from hafnium isotopes in single detrital zircons. Nature, 399(6733): 252–255.https://doi.org/10.1038/20426

Andersen, T., 2002. Correction of common lead in U–Pb analyses that do not report 204Pb. Chemical Geology, 192(1): 59-79.https://doi.org/10.1016/S0009-2541(02)00195-X

Arndt, N.T., Goldstein, S.L., 1987. Use and abuse of crust-formation ages. Geology, 15(10): 893–895.https://doi.org/10.1130/0091-7613(1987)15<893:UAAOCA>2.0.CO;2

Bao, H.T., Wang, Y., Cao, Y.H., 2020. Compositions of the olivine from the Poyi ultramafic intrusion in the Beishan area, Xinjiang: Constraints on the nature of its mantle source. Geochimica, 49(4): 353–367.https://doi.org/10.19700/j.0379-1726.2020.04.001

Barry, T.L., Saunders, A.D., Kempton, P.D., Windley, B.F., Pringle, M.S., Dorjnamjaa, D., Saandar, S., 2003. Petrogenesis of Cenozoic Basalts from Mongolia: Evidence for the Role of Asthenospheric versus Metasomatized Lithospheric Mantle Sources. Journal of Petrology, 44(1): 55–91.https://doi.org/10.1093/petrology/44.1.55

Boyd, F.R., 1989. Compositional distinction between oceanic and cratonic lithosphere. Earth and Planetary Science Letters, 96(1): 15–26.https://doi.org/10.1016/0012-821X(89)90120-9

Brooks, C.K., 1970. The concentrations of zirconium and hafnium in some igneous and metamorphic rocks and minerals. Geochimica et Cosmochimica Acta, 34(3): 411–416.https://doi.org/10.1016/0016-7037(70)90117-1

Bryant, C.J., Arculus, R.J., Chappell, B.W., 1997. Clarence River Supersuite: 250 Ma Cordilleran Tonalitic I-type Intrusions in Eastern Australia. Journal of Petrology, 38(8): 975–1001.https://doi.org/10.1093/petroj/38.8.975

Chai, G., Naldrett, A.J., 1992. The Jinchuan Ultramafic Intrusion–Cumulate of a High-Mg Basaltic Magma. Journal of Petrology, 33(2): 277–303.https://doi.org/10.1093/petrology/33.2.277

Cheng, Z., Guo, Z., 2017. Post-collisional ultrapotassic rocks and mantle xenoliths in the Sailipu volcanic field of Lhasa terrane, south Tibet: Petrological and geochemical constraints on mantle source and geodynamic setting. Gondwana Research, 46: 17–42.https://doi.org/10.1016/j.gr.2017.02.008

Condon, D., Zhu, M.Y., Bowring, S., Wang, W., Yang, A.H., Jin, Y.G., 2005. U-Pb Ages from the Neoproterozoic Doushantuo Formation, China. Science, 308(5718): 95–98.https://doi.org/10.1126/science.1107765

Dandar, O., Okamoto, A., Uno, M., Oyanagi, R., Nagaya, T., Burenjargal, U., Miyamoto, T., Tsuchiya, N., 2019. Formation of secondary olivine after orthopyroxene during hydration of mantle wedge: evidence from the Khantaishir Ophiolite, western Mongolia. Contributions to Mineralogy and Petrology, 174(11): 86.https://doi.org/10.1007/s00410-019-1623-1

Dewey, J.F., Shackleton, R.M., Chengfa, C., Yiyin, S., 1988. The Tectonic Evolution of the Tibetan Plateau. Philosophical Transactions of the Royal Society of London A Mathematical Physical & Engineering Sciences, 327(1594): 379–413.https://doi.org/10.1098/rsta.1988.0135

Dostal, J., Chatterjee, A.K., 1995. Origin of topaz-bearing and related peraluminous granites of the Late Devonian Davis Lake pluton, Nova Scotia, Canada: crystal versus fluid fractionation. Chemical Geology, 123(1): 67–88.https://doi.org/10.1016/0009-2541(95)00047-P

Elliott, T., 2003. Tracers of the slab. American Geophysical Union Geophysical Monograph Series, Washington DC, 23–45 pp.https://doi.org/10.1029/138GM03

Fang, X.Y., Peng, T.P., Fan, W.M., Gao, J.F., Liu, B.B., Zhang, J.Y., 2017. Origin of the Middle-Late Triassic intermediate-acid intrusive rocks in the Yidun terrane and its geological significance. Geochimica, 46(5): 413–434.https://doi.org/10.19700/j.0379-1726.2017.05.002

Fisher, C.M., Vervoort, J.D., Hanchar, J.M., 2014. Guidelines for reporting zircon Hf isotopic data by LA-MC-ICPMS and potential pitfalls in the interpretation of these data. Chemical Geology, 363: 125–133.https://doi.org/10.1016/j.chemgeo.2013.10.019

Gill, J., Condomines, M., 1992. Short-Lived Radioactivity and Magma Genesis. Science, 257(5075): 1368–1376.https://doi.org/10.1126/science.257.5075.1368

Green, D.H., 1975. Genesis of Archean Peridotitic Magmas and Constraints on Archean Geothermal Gradients and Tectonics. Geology, 3(1): 15–18.https://doi.org/10.1130/0091-7613(1975)3<15:GOAPMA>2.0.CO;2

Guo, Z., Marjorie, W., Zhang, M., Cheng, Z., Zhang, L., 2015. Post-collisional Ultrapotassic Mafic Magmatism in South Tibet: Products of Partial Melting of Pyroxenite in the Mantle Wedge Induced by Roll-back and Delamination of the Subducted Indian Continental Lithosphere Slab. Journal of Petrology, 56(7): 1365–1406.https://doi.org/10.1093/petrology/egv040

Hartmann, L.A., Medeiros, J.T.N., Baggio, S.B., Antunes, L.M., 2015. Controls on prolate and oblate geode geometries in the Veia Alta basalt flow, largest world producer of amethyst, Paraná volcanic province, Brazil. Ore Geology Reviews, 66: 243–251.https://doi.org/10.1016/j.oregeorev.2014.11.005

He, D.F., Zhu, W.G., Zhong, H., Ren, T., Bai, Z.J., Fan, H.P., 2013. Zircon U–Pb geochronology and elemental and Sr–Nd–Hf isotopic geochemistry of the Daocheng granitic pluton from the Yidun Arc, SW China. Journal of Asian Earth Sciences, 67-68: 1–17.https://doi.org/10.1016/j.jseaes.2013.02.002

Hoskin, P.W.O., Black, L.P., 2000. Metamorphic zircon formation by solid-state recrystallization of protolith igneous zircon. Journal of Metamorphic Geology, 18(4): 423–439.https://doi.org/10.1046/j.1525-1314.2000.00266.x

Hou, Z., Zaw, K., Pan, G., Mo, X., Xu, Q., Hu, Y., Li, X., 2007. Sanjiang Tethyan metallogenesis in S.W. China: Tectonic setting, metallogenic epochs and deposit types. Ore Geology Reviews, 31(1): 48–87.https://doi.org/10.1016/j.oregeorev.2004.12.007

Hu, P., Li, C., Wang, M., Xie, C., Wu, Y., 2013. Cambrian volcanism in the Lhasa terrane, southern Tibet: Record of an early Paleozoic Andean-type magmatic arc along the Gondwana proto-Tethyan margin. Journal of Asian Earth Sciences, 77: 91–107.https://doi.org/10.1016/j.jseaes.2013.08.015

Hu, P.Y., Li, C., Li, Q.L., Xie, C.M., Wu, Y.W., 2009. Geochemical characteristics of Early Palaeozoic plagioclase granite from ophiolitic cumulate in central Qiangtang, northern Tibet, China. Geological Bulletin of China, 28(9): 1297–1308

Hu, P.Y., Li, C., Wu, Y.W., Xie, C.M., Wang, M., Li, j., 2014. Opening of the Longmu Co-Shuanghu-Lancangjiang ocean: Constraints from plagiogranites. Chinese Science Bulletin, 59: 3188–3199.https://doi.org/10.1007/s11434-014-0434-z

Hu, Z., Liu, Y., Gao, S., Liu, W., Zhang, W., Tong, X., Lin, L., Zong, K., Li, M., Chen, H., Zhou, L., Yang, L., 2012. Improved in situ Hf isotope ratio analysis of zircon using newly designed X skimmer cone and jet sample cone in combination with the addition of nitrogen by laser ablation multiple collector ICP-MS. Journal of

Analytical Atomic Spectrometry, 27(9): 1391–1399.https://doi.org/10.1039/C2JA30078H

Hu, Z., Zhang, W., Liu, Y., Gao, S., Li, M., Zong, K., Chen, H., Hu, S., 2015. "Wave" Signal-Smoothing and Mercury-Removing Device for Laser Ablation Quadrupole and Multiple Collector ICPMS Analysis: Application to Lead Isotope Analysis. Analytical Chemistry, 87(2): 1152–1157

Huang, B., Yan, Y., Piper, J.D.A., Zhang, D., Yi, Z., Yu, S., Zhou, T., 2018. Paleomagnetic constraints on the paleogeography of the East Asian blocks during Late Paleozoic and Early Mesozoic times. Earth Science Reviews, 186: 8–36.https://doi.org/10.1016/j.earscirev.2018.02.004

Iizuka, T., Komiya, T., Johnson, S.P., Kon, Y., Maruyama, S., Hirata, T., 2009. Reworking of Hadean crust in the Acasta gneisses, northwestern Canada: Evidence from in-situ Lu–Hf isotope analysis of zircon. Chemical Geology, 259(3): 230–239.https://doi.org/10.1016/j.chemgeo.2008.11.007

Jia, L., Meng, F., Feng, H., 2018. The Wenquan ultramafic rocks in the Central East Kunlun Fault zone, Qinghai-Tibet Plateau—crustal relics of the Paleo-Tethys ocean. Mineralogy and Petrology, 112(3): 317–339.https://doi.org/10.1007/s00710-017-0544-9

Jian, P., Liu, D., Kröner, A., Zhang, Q., Wang, Y., Sun, X., Zhang, W., 2009a. Devonian to Permian plate tectonic cycle of the Paleo-Tethys Orogen in southwest China (I): Geochemistry of ophiolites, arc/back-arc assemblages and within-plate igneous rocks. Lithos, 113(3): 748–

766.https://doi.org/10.1016/j.lithos.2009.04.004

Jian, P., Liu, D., Kröner, A., Zhang, Q., Wang, Y., Sun, X., Zhang, W., 2009b. Devonian to Permian plate tectonic cycle of the Paleo-Tethys Orogen in southwest China (II): Insights from zircon ages of ophiolites, arc/back-arc assemblages and within-plate igneous rocks and generation of the Emeishan CFB province. Lithos, 113(3): 767–784.https://doi.org/10.1016/j.lithos.2009.04.006

Jian, P., Liu, D., Sun, X., 2008. SHRIMP dating of the Permo-Carboniferous Jinshajiang ophiolite, southwestern China: Geochronological constraints for the evolution of Paleo-Tethys. Journal of Asian Earth Sciences, 32(5): 371–384.https://doi.org/10.1016/j.jseaes.2007.11.006

Jiang, S.Y., Wang, R.C., Xu, X.S., Zhao, K.D., 2005. Mobility of high field strength elements (HFSE) in magmatic-, metamorphic-, and submarine-hydrothermal systems. Physics and Chemistry of the Earth, 30(17-18): 1020–1029.https://doi.org/10.1016/j.pce.2004.11.004

Johnson, M.C., Plank, T., 2000. Dehydration and melting experiments constrain the fate of subducted sediments. Geochemistry, Geophysics, Geosystems 1(12).https://doi.org/10.1029/1999GC000014

Kamenetsky, V.S., Elburg, M., Arculus, R., Thomas, R., 2006. Magmatic origin of low-Ca olivine in subduction-related magmas: Co-existence of contrasting magmas. Chemical Geology, 233(3): 346–357.https://doi.org/10.1016/j.chemgeo.2006.03.010

Leng, C.B., Huang, Q.Y., Zhang, X.C., Wang, S.X., Zhong, H., Hu, R.Z., Bi, X.W., Zhu, J.J., Wang, X.S., 2014. Petrogenesis of the Late Triassic volcanic rocks in the Southern Yidun arc, SW China: Constraints from the geochronology, geochemistry, and Sr–Nd–Pb–Hf isotopes. Lithos, 190–191: 363–382.https://doi.org/10.1016/j.lithos.2013.12.018

Li, C., Dong, Y.S., Zhai, Q.G., Wang, L.Q., Yan, Q.R., Wu, Y.W., He, T.T., 2008. Discovery of Eopaleozoic ophiolite in the Qiangtang of Tibet Plateau: Evidence from SHRIMP U-Pb dating and its tectonic implications. Acta Petrologiea Sinica, 24(1): 31–36

Li, S.Z., Zhao, S.J., Li, X.Y., Cao, H.H., Liu, X., Guo, X.Y., Xiao, W.J., Lai, S.C., Yan, Z., Li, Z.H., Yu, S.Y., Lan, H.Y., 2016a. Proto-Tehtys Ocean in East Asia (Ⅰ): Northern and southern border faults and subduction polarity. Acta Petrologica Sinica, 32(9): 2609–2627

Li, S.Z., Zhao, S.J., Yu, S., Cao, H.H., Li, X.Y., Liu, X., Guo, X.Y., Xiao, W.J., Lai, S.C., Yan, Z., Li, Z.H., Yu, S.Y., Zhang, J., Lan, H.Y., 2016b. Proto-Tehtys Ocean in East Asia (Ⅱ): Affinity and assmbly of Early Paleozoic micro-continental blocks. Acta Petrologica Sinica, 32(9): 2628–2644

Li, W., Yu, H., Gao, X., Liu, X., Wang, J., 2017. Review of Mesozoic multiple magmatism and porphyry Cu–Mo (W) mineralization in the Yidun Arc, eastern Tibet Plateau. Ore Geology Reviews, 90: 795–812.https://doi.org/10.1016/j.oregeorev.2017.03.009

Li, W.C., Yin, G.H., Lu, Y.X., Wang, Y.B., Yu, H.J., Cao, X.M., Zhang, S.Q., 2010. Delineation of Hongshan-Shudu ophiolite melange in Geza volcanic-magmatic arc and its significance, southwest "Jinsha-Lancang-Nu rivers". Acta Petrologica Sinica, 26(6): 1661–1671

Liu, B., Ma, C.Q., Guo, Y.H., Xiong, F.H., Guo, P., Zhang, X., 2016a. Petrogenesis and tectonic implications of Triassic mafic complexes with MORB/OIB affinities from the western Garzê-Litang ophiolitic mélange, central Tibetan Plateau. Lithos, 260: 253–267.https://doi.org/10.1016/j.lithos.2016.06.009

Liu, H., Wang, B.D., Chen, L., Huang, F., Zeng, Y.C., Wang, L.Q., 2021. Silurian intermediate-felsic complex in the Xiangtaohu area of central Qiangtang, northern Tibet: Evidence for southward subduction of the Longmuco-Shuanghu Prototethys oceanic plate. Lithos, 404.https://doi.org/10.1016/j.lithos.2021.106465

Liu, Y., Gao, S., Hu, Z., Gao, C., Zong, K., Wang, D., 2009. Continental and Oceanic Crust Recycling-induced Melt–Peridotite Interactions in the Trans-North China Orogen: U–Pb Dating, Hf Isotopes and Trace Elements in Zircons from Mantle Xenoliths. Journal of Petrology, 51(1-2): 537–571.https://doi.org/10.1093/petrology/egp082

Liu, Y., Hu, Z., Gao, S., Günther, D., Xu, J., Gao, C., Chen, H., 2008. In situ analysis of major and trace elements of anhydrous minerals by LA-ICP-MS without applying an internal standard. Chemical Geology, 257(1): 34–43.https://doi.org/10.1016/j.chemgeo.2008.08.004

Liu, Y., Hu, Z., Zong, K., Gao, C., Gao, S., Xu, J., Chen, H., 2010. Reappraisement and refinement of zircon U-Pb isotope and trace element analyses by LA-ICP-MS.

Chinese Science Bulletin, 55(15): 1535–1546.https://doi.org/10.1007/s11434-010-3052-4

Liu, Y., Lü, X., Wu, C., Hu, X., Duan, Z., Deng, G., Wang, H., Zhu, X., Zeng, H., Wang, P., Wang, W., Lu, Q., 2016b. The migration of Tarim plume magma toward the northeast in Early Permian and its significance for the exploration of PGE-Cu–Ni magmatic sulfide deposits in Xinjiang, NW China: As suggested by Sr–Nd–Hf isotopes, sedimentology and geophysical data. Ore Geology Reviews, 72: 538–545.https://doi.org/10.1016/j.oregeorev.2015.07.020

Liu, Y., Xiao, W.J., Windley, B.F., Schulmann, K., Li, R.S., Ji, W.H., Zhou, K.F., Sang, M., Chen, Y.C., Jia, X.L., Li, L., 2019. Late Silurian to Late Triassic seamount/oceanic plateau series accretion in Jinshajiang subduction melange, Central Tibet, SW China. Geological Journal, 54(2): 961–977.https://doi.org/10.1002/gj.3432

Lu, Y., 2004. Geokit—A geochemical toolkit for Microsoft Excel. Geochimica, 33: 459–464

Ludwig, K.R., 2003. ISOPLOT 3.0: A Geochronological Toolkit for Microsoft Excel. Berkeley Geochronology Center Special Publication. US Geol. Sur. Open File Rep., 39, 91–445 pp

Maffione, M., Morris, A., Plümper, O., van Hinsbergen, D.J.J., 2014. Magnetic properties of variably serpentinized peridotites and their implication for the evolution of oceanic core complexes. Geochemistry, Geophysics, Geosystems, 15(4): 923–944.https://doi.org/10.1002/2013GC004993

Mao, X.C., Wang, L.Q., Li, B., Wang, B.D., Wang, D.B., Yin, F.G., Sun, Z.M., 2012. Discovery of the Late Silurian volcanic rocks in the Dazhonghe area, Yunxian-Jinggu volcanic arc belt, western Yunnan, China and its geological significance. Acta Geologica Sinica 28(5): 1517–1528

McDonough, W.F., Sun, S.s., 1995. The composition of the Earth. Chemical Geology, 120(3): 223–253.https://doi.org/10.1016/0009-2541(94)00140-4

McKenzie, D.A.N., O'Nions, R.K., 1991. Partial Melt Distributions from Inversion of Rare Earth Element Concentrations. Journal of Petrology, 32(5): 1021–1091.https://doi.org/10.1093/petrology/32.5.1021

Meng, Y., Santosh, M., Mao, G., Lin, P., Liu, J., Ren, P., 2020. New constraints on the tectono-magmatic evolution of the central Gangdese belt from Late Cretaceous magmatic suite in southern Tibet. Gondwana Research, 80: 123–141.https://doi.org/10.1016/j.gr.2019.10.014

Metcalfe, I., 2021. Multiple Tethyan ocean basins and orogenic belts in Asia. Gondwana Research, 100: 87–130.https://doi.org/10.1016/j.gr.2021.01.012

Morimoto, N., 1988. Nomenclature of Pyroxenes. Mineralogy and Petrology, 39(1): 55–76.https://doi.org/10.1007/BF01226262

Nutman, A.P., Scicchitano, M.R., Friend, C.R.L., Bennett, V.C., Chivas, A.R., 2021. Isua (Greenland) ~3700 Ma meta-serpentinite olivine Mg# and δ18O signatures show connection between the early mantle and hydrosphere: Geodynamic implications. Precambrian Research, 361: 106249.https://doi.org/10.1016/j.precamres.2021.106249

O'Hara, M.J., 1968. Are Ocean Floor Basalts Primary Magma? Nature, 220: 683–686

Ortega-Obregón, C., Solari, L., Gómez-Tuena, A., Elías-Herrera, M., Ortega-Gutiérrez, F., Macías-Romo, C., 2014. Permian–Carboniferous arc magmatism in southern Mexico: U–Pb dating, trace element and Hf isotopic evidence on zircons of earliest subduction beneath the western margin of Gondwana. International Journal of Earth Sciences, 103(5): 1287–1300.https://doi.org/10.1007/s00531-013-0933-1

Pan, G., Wang, L., Li, R., Yuan, S., Ji, W., Yin, F., Zhang, W., Wang, B., 2012. Tectonic evolution of the Qinghai-Tibet Plateau. Journal of Asian Earth Sciences, 53: 3–14.https://doi.org/10.1016/j.jseaes.2011.12.018

Pan, G.T., Lu, S.N., Xiao, Q.H., Zhang, K.X., Yin, F.G., Hao, G.J., Luo, M.S., Ren, F., Yuan, S.H., 2016. Division of tectonic stages and tectonic evolution in China. Earth Science Frontiers, 23(6): 10–23.https://doi.org/10.13745/j.esf.2016.06.001

Pan, G.T., Wang, L.Q., Geng, Q.R., Yin, F.G., Wang, B.D., Wang, D.B., Peng, Z.M., Ren, F., 2020. Space-time structure of the Bangonghu-Shuanghu-Nujiang-Changning-Menglian Mega-suture zone: A discussion on geology and evolution of the Tethys Ocean. Sedimentary Geology and Tethyan Geology, 40(3): 1–19.https://doi.org/10.19826/j.cnki.1009-3850.2020.07001

Pearce, J., 1982. Trace element characteristics of lavas from destructive plate boundaries. In: Thorpe, R.S. (Ed.), Andesites: Orogenic Andesites and Related Rocks. John Wiley and Sons

Pearce, J.A., Cann, J.R., 1973. Tectonic setting of basic volcanic rocks determined using trace element analyses. Earth and Planetary Science Letters, 19(2): 290–300.https://doi.org/10.1016/0012-821X(73)90129-5

Polat, A., Hofmann, A.W., 2003. Alteration and geochemical patterns in the 3.7–3.8 Ga Isua greenstone belt, West Greenland. Precambrian Research, 126(3): 197–218.https://doi.org/10.1016/S0301-9268(03)00095-0

Polat, A., Hofmann, A.W., Rosing, M.T., 2002. Boninite-like volcanic rocks in the 3.7–3.8 Ga Isua greenstone belt, West Greenland: geochemical evidence for intra-oceanic subduction zone processes in the early Earth. Chemical Geology, 184(3): 231–254.https://doi.org/10.1016/S0009-2541(01)00363-1

Prelević, D., Jacob, D.E., Foley, S.F., 2013. Recycling plus: A new recipe for the formation of Alpine–Himalayan orogenic mantle lithosphere. Earth and Planetary Science Letters, 362: 187–197.https://doi.org/10.1016/j.epsl.2012.11.035

Qin, M., Yan, S.T., Wen, L., Tan, C.H., Duan, Y.H., 2019. The tectonic evolution of the Garze-Litang ophiolite mélange zone in the Late Triassic: Constraints from geochronology and geochemistry of the Yongjie batholith in the Garze-Litang area. Geological Bulletin of China, 38(10): 1615–1625

Reid, A.J., Wilson, C., Liu, S., 2005. Structural evidence for the Permo-Triassic tectonic evolution of the Yidun Arc, eastern Tibetan Plateau. Journal of Structural Geology, 27(1): 119–137.https://doi.org/10.1016/j.jsg.2004.06.011

Roeder, P.L., Emslie, R.F., 1970. Olivine-liquid equilibrium. Contributions to

Mineralogy and Petrology, 29(4): 275–289.https://doi.org/10.1007/BF00371276

Roger, F., Jolivet, M., Malavieille, J., 2010. The tectonic evolution of the Songpan-Garzê (North Tibet) and adjacent areas from Proterozoic to Present: A synthesis. Journal of Asian Earth Sciences, 39(4): 254–269.https://doi.org/10.1016/j.jseaes.2010.03.008

Rooney, T., Furman, T., Bastow, I., Ayalew, D., Yirgu, G., 2007. Lithospheric modification during crustal extension in the Main Ethiopian Rift. Journal of Geophysical Research Solid Earth, 112(B10): 1–8.https://doi.org/10.1029/2006JB004916

Rosenstengel, L.M., Hartmann, L.A., 2012. Geochemical stratigraphy of lavas and fault-block structures in the Ametista do Sul geode mining district, Paraná volcanic province, southern Brazil. Ore Geology Reviews, 48: 332–348.https://doi.org/10.1016/j.oregeorev.2012.05.003

Sengör, A.M.C., 1984. The Cimmeride Orogenic System and the Tectonics of Eurasia, 195. Geological Society of America.https://doi.org/10.1130/spe195

Sheldrick, T.C., Barry, T.L., Van Hinsbergen, D.J.J., Kempton, P.D., 2018. Constraining lithospheric removal and asthenospheric input to melts in Central Asia: A geochemical study of Triassic to Cretaceous magmatic rocks in the Gobi Altai (Mongolia). Lithos, 296-299: 297–315.https://doi.org/10.1016/j.lithos.2017.11.016

Simkin, T., Smith, J.V., 1970. Minor-Element Distribution in Olivine. The Journal of

Geology, 78(3): 304–325.https://doi.org/10.1086/627519
Su, B.X., Qin, K.Z., Sakyi, P.A., Li, X.H., Yang, Y.H., Sun, H., Tang, D.M., Liu, P.P., Xiao, Q.H., Malaviarachchi, S.P.K., 2011. U–Pb ages and Hf–O isotopes of zircons from Late Paleozoic mafic–ultramafic units in the southern Central Asian Orogenic Belt: Tectonic implications and evidence for an Early-Permian mantle plume. Gondwana Research, 20(2): 516–531.https://doi.org/10.1016/j.gr.2010.11.015
Sun, H., Qin, K.Z., Su, B.X., Fan, X., Tang, D.M., Li, J., 2009. Discovery of komatitic ultramaic intrusion in Mid-Tianshanterrain: Xiadong intrusion, Xinjiang. Acta Petrologica Sinica, 25(4): 738–748
Sun, S.S., McDonough, W.E., 1989. Chemical and isotopic systematics of oceanic basalts: Implications for mantlecomposition and processes. Magmatism in the Oceanic Basins, 42. Geological Society, London, Special Publications, 313–345 pp.http://dx.doi.org/10.1144/GSL.SP.1989.042.01.19
Sun, Z.B., Zeng, W.T., Zhou, K., Wu, J.L., Li, G.J., Huang, L., Zhao, J.T., 2017. Identification of Ordovician oceanic island basalt in the Changning-Menglian suture zone and its tectonic implications: Evidence from geochemical and geochronological data. Geological Bulletin of China, 36(10): 1760–1771
Tang, Y.J., Zhang, H.F., Ying, J.F., Zhang, J., Liu, X.M., 2008. Refertilization of ancient lithospheric mantle beneath the central North China Craton: Evidence from petrology and geochemistry of peridotite xenoliths. Lithos, 101(3): 435–452.https://doi.org/10.1016/j.lithos.2007.09.006

Tang, Y.J., Zhang, H.F., Ying, J.F., 2004. High-Mg olivine xenocrysts entrained in Cenozoic basalts in central Taihang Mountains: relicts of old lithospheric mantle. Acta Petrologica Sinica, 20(5): 1243–1252

Tang, Y.J., Zhang, H.F., Ying, J.F., Su, B.X., Chu, Z.Y., Xiao, Y., Zhao, X.M., 2013. Highly heterogeneous lithospheric mantle beneath the Central Zone of the North China Craton evolved from Archean mantle through diverse melt refertilization. Gondwana Research, 23(1): 130–140.https://doi.org/10.1016/j.gr.2012.01.006

Tian, Z.D., Leng, C.B., Zhang, X.C., 2020. Provenance and tectonic setting of the Neoproterozoic meta-sedimentary rocks at southeastern Tibetan Plateau: Implications for the tectonic affinity of Yidun terrane. Precambrian Research, 344: 105736.https://doi.org/10.1016/j.precamres.2020.105736

Tian, Z.D., Leng, C.B., Zhang, X.C., Tian, F., Lai, C.K., 2022. Late Neoproterozoic-early Paleozoic tectonic evolution and paleogeographic reconstruction of the eastern Tibetan Plateau: A perspective from detrital zircon U–Pb-Hf isotopic evidence. Precambrian Research, 377: 106738.https://doi.org/10.1016/j.precamres.2022.106738

Vervoort, J.D., Jonathan Patchett, P., 1996. Behavior of hafnium and neodymium isotopes in the crust: Constraints from Precambrian crustally derived granites. Geochimica et Cosmochimica Acta, 60(19): 3717–3733.https://doi.org/10.1016/0016-7037(96)00201-3

Wang, B.D., Wang, L.Q., Chung, S.L., Chen, J.L., Yin, F.G., Liu, H., Li, X.B., Chen, L.K., 2016a. Evolution of the Bangong–Nujiang Tethyan ocean: Insights from the geochronology and geochemistry of mafic rocks within ophiolites. Lithos, 245: 18–33.https://doi.org/10.1016/j.lithos.2015.07.016

Wang, B.D., Wang, L.Q., Pan, G.T., Yin, F.G., Wang, D.B., Tang, Y., 2013. U-Pb zircon dating of Early Paleozoic gabbro from the Nantinghe ophiolite in the Changning-Menglian suture zone and its geological implication. Chinese Science Bulletin, 58: 344–354.https://doi.org/10.1007/s11434-012-5481-8

Wang, B.D., Wang, L.Q., Wang, D., Li, F.Q., Tang, Y., Wang, Q.Y., Yan, G.C., Wu, Z., 2021. The temporal and spatial framework and its tectonic evolution of the Jinsha River arc-basin system, Southwest China. Sedimentary Geology and Tethyan Geology, 41(2): 247–264

Wang, D.B., Luo, L., Tang, Y., Yin, F.G., Wang, B.D., Wang, L.Q., 2016b. Zircon U-Pb dating and petrogenesis of Early Paleozoic adakites from the Niujingshan ophiolitic mélange in the Changning-Menglian suture zone and its geological implications. Acta Petrologica Sinica, 32(8): 2317–2329

Wang, D.B., Wang, L.Q., Yin, F.G., Sun, Z.M., Wang, B.D., Zhang, W.P., 2012. Timing and nature of the Jinshajiang Paleo-Tethys: Constraints from zircon U-Pb age and Hf isotope of the Dongzhulin layered gabbro from Jinshajiang ophiolite belt, northwestern Yunnan. Acta Petrologica Sinica, 28(5): 1542–1550

Wang, H., Liu, F., Li, J., Sun, Z., Santosh, M., 2019a. Petrology, geochemistry and P–T–t path of lawsonite-bearing retrograded eclogites in the Changning–Menglian orogenic belt, southeast Tibetan Plateau. Journal of Metamorphic Geology, 37: 439–478.https://doi.org/10.1111/jmg.12462

Wang, H., Zhai, Q., Hu, P., Zeng, L., Tang, Y., Zhu, Z., 2020a. Early Paleozoic granitic rocks of the South Qiangtang Terrane, northern Tibetan Plateau: Implications for subduction of the Proto- (Paleo-) Tethys Ocean. Journal of Asian Earth Sciences, 204: 104579.https://doi.org/10.1016/j.jseaes.2020.104579

Wang, H.T., Zhai, Q.G., Hu, P.Y., Zeng, L.S., Tang, Y., Zhu, Z.C., 2020b. Late Cambrian to Early Silurian Granitic Rocks of the Gemuri Area, Central Qiangtang, North Tibet: New Constraints on the Tectonic Evolution of the Northern Margin of Gondwana. Acta Geologica Sinica 94(4): 1007–1019.https://doi.org/10.1111/1755-6724.14556

Wang, J.P., Li, X.W., Ning, W.B., Kusky, T.M., Wang, L., Polat, A., Deng, H., 2019b. Geology of a Neoarchean suture: Evidence from the Zunhua ophiolitic melange of the Eastern Hebei Province, North China Craton. Geological Society of America Bulletin, 131(11-12): 1943–1964.https://doi.org/10.1130/B35138.1

Wang, L.Q., Pan, G.T., Li, C., Dong, Y.S., Zhu, D.C., Yuan, S.H., Zhu, T.X., 2008. SHRIMP U-Pb zircon dating of Eopaleozoic cumulatein Guoganjianian Mt.from central Qiangtang area of northern Tibet-Considering the evolvement of Proto-and Paleo-Tethys. Geological Bulletion of China, 27(12): 2045–2056

Wang, X., Griffin, W.L., Chen, J., 2010. Hf contents and Zr/Hf ratios in granitic zircons. Geochemical Journal, 44(1): 65–72.https://doi.org/10.2343/geochemj.1.0043

Wedepohl, K.H., 1995. The composition of the continental crust. Geochimica et Cosmochimica Acta, 59(7): 1217–1232.https://doi.org/10.1016/0016-7037(95)00038-2

Winchester, J.A., Floyd, P.A., 1977. Geochemical discrimination of different magma series and their differentiation products using immobile elements. Chemical Geology, 20: 325–343.https://doi.org/10.1016/0009-2541(77)90057-2

Woodhead, J.D., Hergt, J.M., Davidson, J.P., Eggins, S.M., 2001. Hafnium isotope evidence for 'conservative' element mobility during subduction zone processes. Earth and Planetary Science Letters, 192(3): 331–346.https://doi.org/10.1016/S0012-821X(01)00453-8

Wu, F., Li, X., Zheng, Y., Gao, S., 2007. Lu–Hf isotopic systematics and their applications in petrology. Acta Petrologica Sinica 23(2): 185–220

Wu, F., Wan, B., Zhao, L., Xiao, W., Zhu, R., 2020. Tethyan geodynamics. Acta Petrologica Sinica, 36(6): 1627–1674.https://doi.org/10.18654/1000-0569/2020.06.01

Wu, T., Xiao, L., Ma, C., 2016a. U-Pb geochronology of detrital and inherited zircons in the Yidun arc belt, eastern Tibet Plateau and its tectonic implications. Journal of Earth Science, 27(3): 461–473.https://doi.org/10.1007/s12583-016-0675-5

Wu, Y.W., Li, C., Xu, M.J., Xiong, S.Q., Wang, M., 2016b. Petrology and geochemistry of metabasalts from the Taoxinghu Ophiolite, Central Giangtang, Northern Tibet: Evidence for a continental back-arc basin system. Austrian Journal of Earth Sciences, 109(2): 166–177.https://doi.org/10.17738/ajes.2016.0012

Xu, W., Yang, D., Gao, S., Pei, F., Yu, Y., 2010. Geochemistry of peridotite xenoliths in Early Cretaceous high-Mg# diorites from the Central Orogenic Block of the North China Craton: The nature of Mesozoic lithospheric mantle and constraints on lithospheric thinning. Chemical Geology, 270(1): 257–273.https://doi.org/10.1016/j.chemgeo.2009.12.006

Xu, X., Wen, X., Yu, G., Zheng, R., Luo, H., Zheng, B., 2005. Average slip rate, earthquake rupturing segmentation and recurrence behavior on the Litang fault zone, western Sichuan Province, China. Science in China Series D: Earth Sciences, 48(8): 1183–1196.https://doi.org/10.1360/04yd0072

Xu, X.B., Xia, Y., Chen, J.J., Liang, C.H., Xu, Y.D., 2021. Late Triassic foreland basin and Early Palaeozoic basement in the eastern Yidun Micro-block and its tectonic implications for the eastern Palaeo-Tethys. Geological Journal, 56(11): 5821–5838.https://doi.org/10.1002/gj.4277

Yakymchuk, C., Kirkland, C.L., Clark, C., 2018. Th/U ratios in metamorphic zircon. Journal of Metamorphic Geology, 36(6): 715–737.https://doi.org/10.1111/jmg.12307

Yan, Q.R., Wang, Z.Q., Liu, S.W., Li, Q.G., Zhang, H.Y., Wang, T., Liu, D.Y., Shi, Y.R., Jian, P., Wang, J.G., Zhang, D.H., Zhao, J., 2005. Opening of the Tethys in southwest China and its significance to the breakup of East Gondwanaland in late Paleozoic: Evidence from SHRIMP U-Pb zircon analyses for the Garze ophiolite block. Chinese Science Bulletin, 50(3): 256–264.https://doi.org/10.1007/BF02897536

Zhai, Q.G., Jahn, B.M., Wang, J., Hu, P.Y., Chung, S.L., Lee, H.Y., Tang, S.H., Tang, Y., 2016. Oldest Paleo-Tethyan ophiolitic mélange in the Tibetan Plateau. Geological Society of America Bulletin 128(3-4): 355–

373.https://doi.org/10.1130/B31296.1

Zhai, Q.G., Jahn, B.M., Wang, J., Su, L., Mo, X.X., Wang, K.L., Tang, S.H., Lee, H.Y., 2013. The Carboniferous ophiolite in the middle of the Qiangtang terrane, Northern Tibet: SHRIMP U–Pb dating, geochemical and Sr–Nd–Hf isotopic characteristics. Lithos, 168-169: 186–199.https://doi.org/10.1016/j.lithos.2013.02.005

Zhai, Q.G., Wang, J., Li, C., Su, L., 2010. SHRIMP U-Pb dating and Hf isotopic analyses of Middle Ordovician meta-cumulate gabbro in central Qiangtang, northern Tibetan Plateau. Sci China Earth Sci, 53: 657–664.https://doi.org/10.1007/s11430-010-0063-6

Zhang, H., Zhang, H., Zou, D., 2021. Comprehensive refertilization of the Archean–Paleoproterozoic lithospheric mantle beneath the northwestern North China Craton: Evidence from in situ Sr isotopes of the Siziwangqi peridotites. Lithos, 380–381: 105822.https://doi.org/10.1016/j.lithos.2020.105822

Zhang, T.Y., Li, C., L, S., Xie, C.M., Wu, Y.W., Wang, M., 2014. LA-ICP-MS zircon U-Pb ages and geochemical characteristics of cumulates in the Riwanchaka area, middle Qiangtang, the Tibetan Plateau. Geological Bulletin of China, 33(11): 1662–1672

Zhao, G., Wang, Y., Huang, B., Dong, Y., Li, S., Zhang, G., Yu, S., 2018. Geological reconstructions of the East Asian blocks: From the breakup of Rodinia to the assembly of Pangea. Earth-Science Reviews, 186: 262–286.https://doi.org/10.1016/j.earscirev.2018.10.003

Zhao, J.H., Zhou, M.F., 2007. Geochemistry of Neoproterozoic mafic intrusions in the Panzhihua district (Sichuan Province, SW China): Implications for subduction-related metasomatism in the upper mantle. Precambrian Research, 152(1-2): 27–47.https://doi.org/10.1016/j.precamres.2006.09.002

Zhao, S.W., Lai, S.C., Gao, L., Qin, J.F., Zhu, R.Z., 2016. Evolution of the Proto-Tethys in the Baoshan block along the East Gondwana margin: constraints from early Palaeozoic magmatism. International Geology Review, 59(1): 1–15.https://doi.org/10.1080/00206814.2016.1198994

Zhao, T., Sun, F., Peng, B., Wang, C., 2020. Timing of formation of the Western Jinshajiang and Ganzê–Litang sutures: evidence from the Duocai Granite in the Zhiduo region, West China. Acta Geochimica, 39(5): 741–759.https://doi.org/10.1007/s11631-020-00408-4

Zhao, T.Y., Feng, Q.L., Metcalfe, I., Milan, L.A., Liu, G.C., Zhang, Z.B., 2017. Detrital zircon U-Pb-Hf isotopes and provenance of Late Neoproterozoic and Early Paleozoic sediments of the Simao and Baoshan blocks, SW China: Implications for Proto-Tethys and Paleo-Tethys evolution and Gondwana reconstruction. Gondwana Research, 51: 193–208.https://doi.org/10.1016/j.gr.2017.07.012

Zheng, J., O'Reilly, S.Y., Griffin, W.L., Lu, F., Zhang, M., Pearson, N.J., 2001. Relict refractory mantle beneath the eastern North China block: significance for lithosphere evolution. Lithos, 57(1): 43–66.https://doi.org/10.1016/S0024-4937(00)00073-6

Zhu, D., Zhao, Z., Niu, Y., Dilek, Y., Hou, Z., Mo, X., 2013. The origin and pre-

Cenozoic evolution of the Tibetan Plateau. Gondwana Research, 23(4): 1429–1454.https://doi.org/10.1016/j.gr.2012.02.002

Zi, J.W., Cawood, P.A., Fan, W.M., Wang, Y.J., Tohver, E., 2012. Contrasting rift and subduction-related plagiogranites in the Jinshajiang ophiolitic melange, southwest China, and implications for the Paleo-Tethys. Tectonics, 31(2): 1–18.https://doi.org/10.1029/2011TC002937

Figures

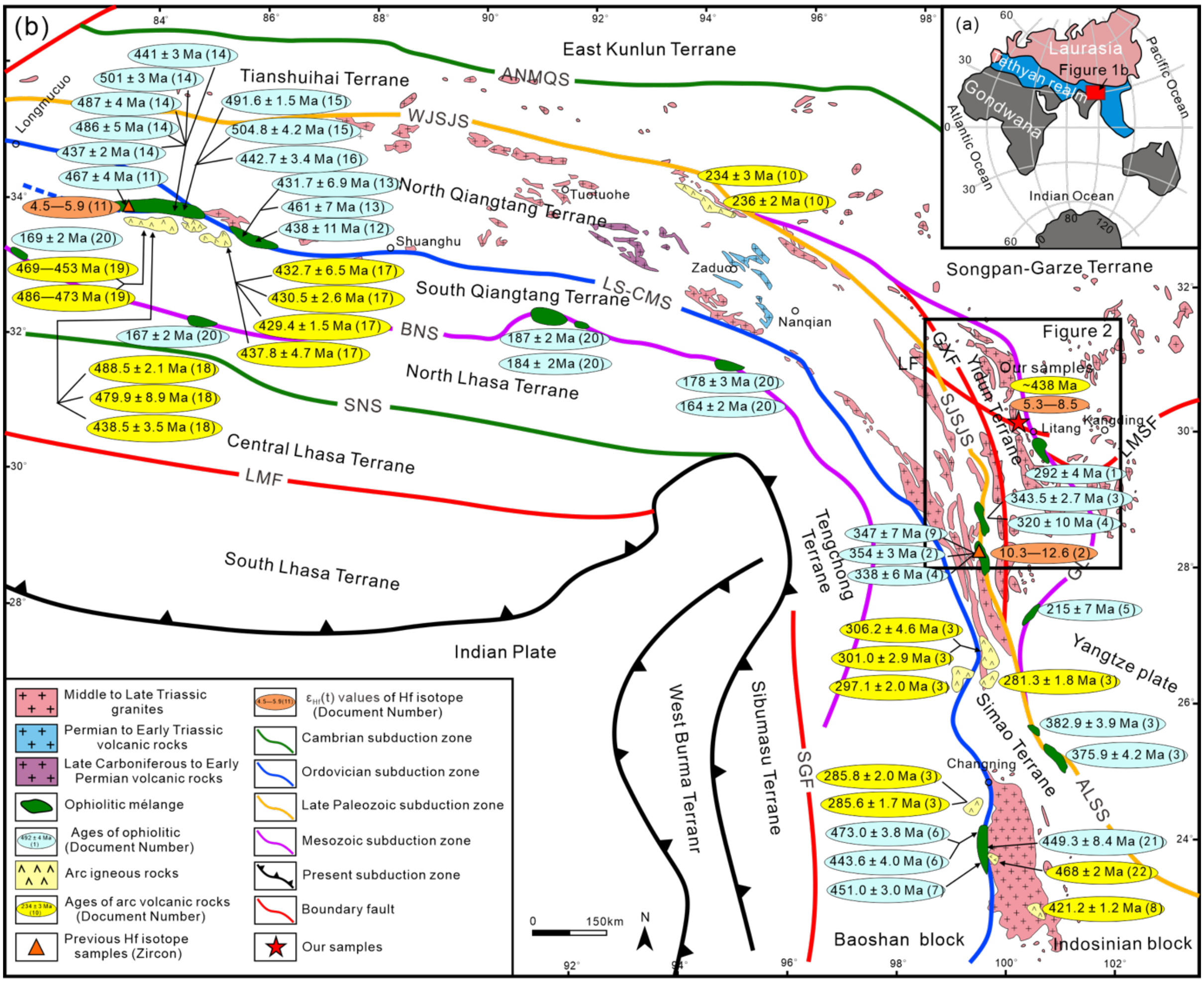

Figure 1. (a) Location of the Tibetan Plateau in the Tethyan realm modified from Liu et al. (2016a). (b) Simplified geological map of the Tibetan Plateau. The numbered key (in Figure b) reflects data from: (1) Yan et al. (2005); (2) Wang et al. (2012); (3) Jian et al. (2009b); (4) Jian et al. (2008); (5) Li et al. (2010); (6) Wang et al. (2013); (7) Wang et al. (2019a); (8) Mao et al. (2012); (9) Zi et al. (2012); (10) (Liu et al., 2016a); (11) Zhai et al. (2010); (12) Li et al. (2008); (13) Wang et al. (2008); (14) Zhai et al. (2016); (15) Hu et al. (2014); (16) Zhang et al. (2014); (17) Liu et al. (2021); (18) Wang et al. (2020b); (19) Wang et al. (2020a); (20) Wang et al. (2016a); (21) Sun et al. (2017); (22) Wang et al. (2016b). ANMQS = Animaqing suture zone; WJSJS = Western Jinshajiang suture zone; SJSJS = Southern Jinshajiang suture zone; GLS = Litang-Garze suture zone; LS-CMS = Longmucuo Shuanghu-Changning Menglian suture

zone; SNS = Bangong Nujiang suture zone; ALSS = Ailaoshan suture zone; LMSF = Longmenshan fault; GXF = Garze-Xiangcheng fault; LF = Litang fault; LMF = Luobadui-Milashan fault; SGF = ShiJie fault.

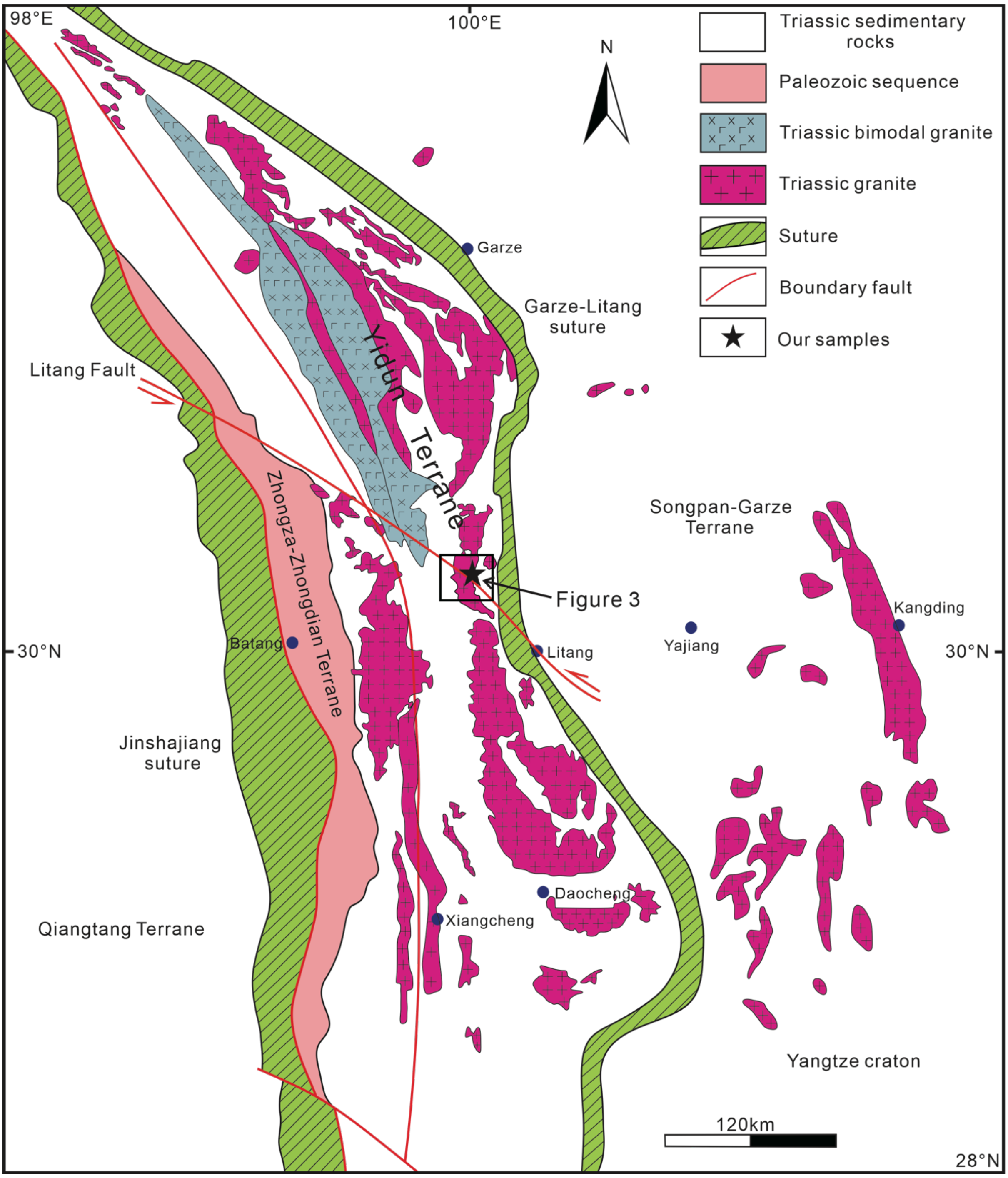

Figure 2. Regional tectonics and location of the west Sichuan and eastern Tibet area, China, after Hou et al. (2007).

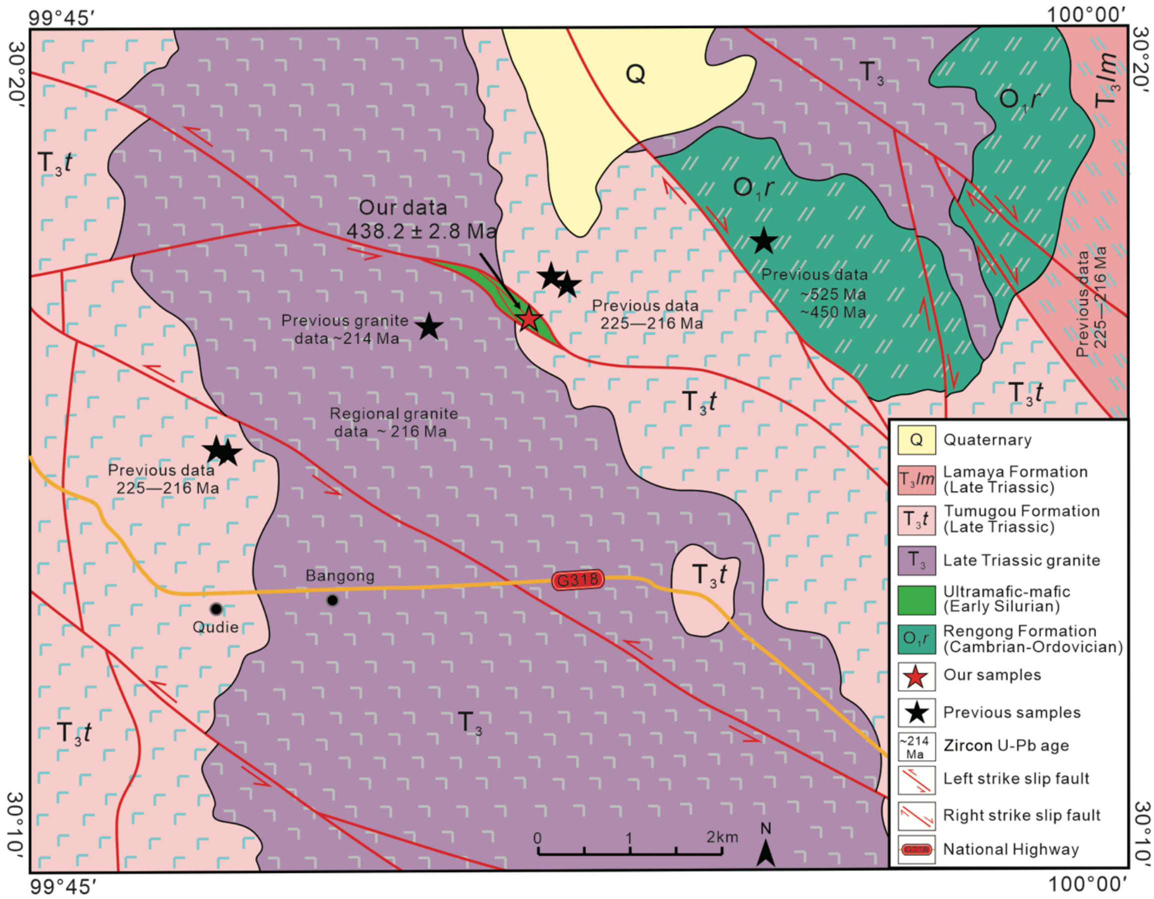

Figure 3. Geological sketch map of the Heni area, eastern Tibet, China. Previous sedimentary rock data and sampling sites were obtained from Xu et al. (2021). Previous granite data was obtained from Qin et al. (2019), and regional igneous rock data from Fang et al. (2017).

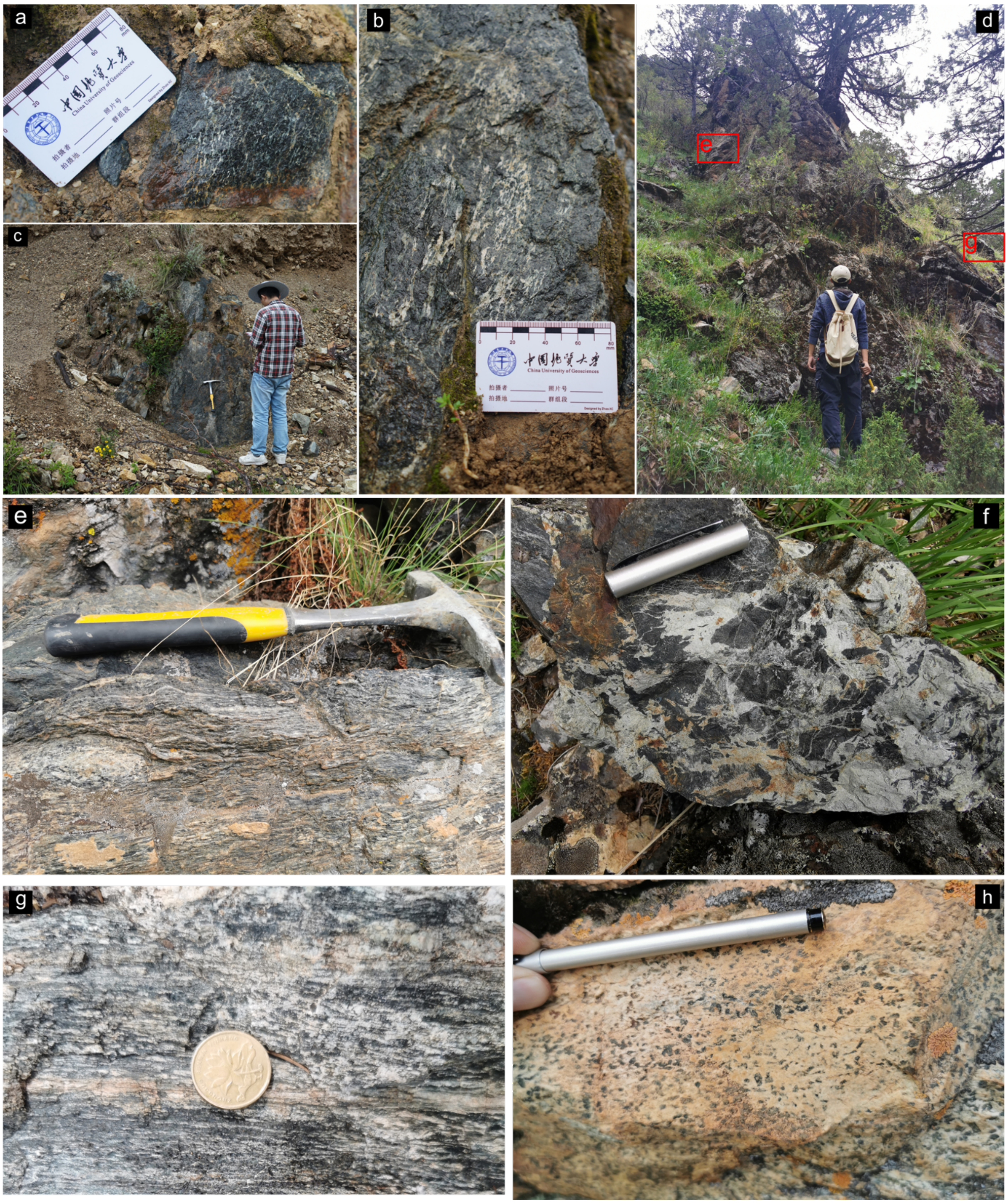

Figure 4. Field photographs of the mafic-ultramafic rocks from the Heni area, eastern Tibet, China: (a-c) Serpentinite and fine-grained peridotite outcrop. (d-f) Meta-gabbro (amphibolite) lenses/blocks in a metasedimentary matrix. (g) Dark colored harzburgite and light-colored melts. (h) Undeformed gabbro, composed of hornblende and pseudo pyroxene crystals.

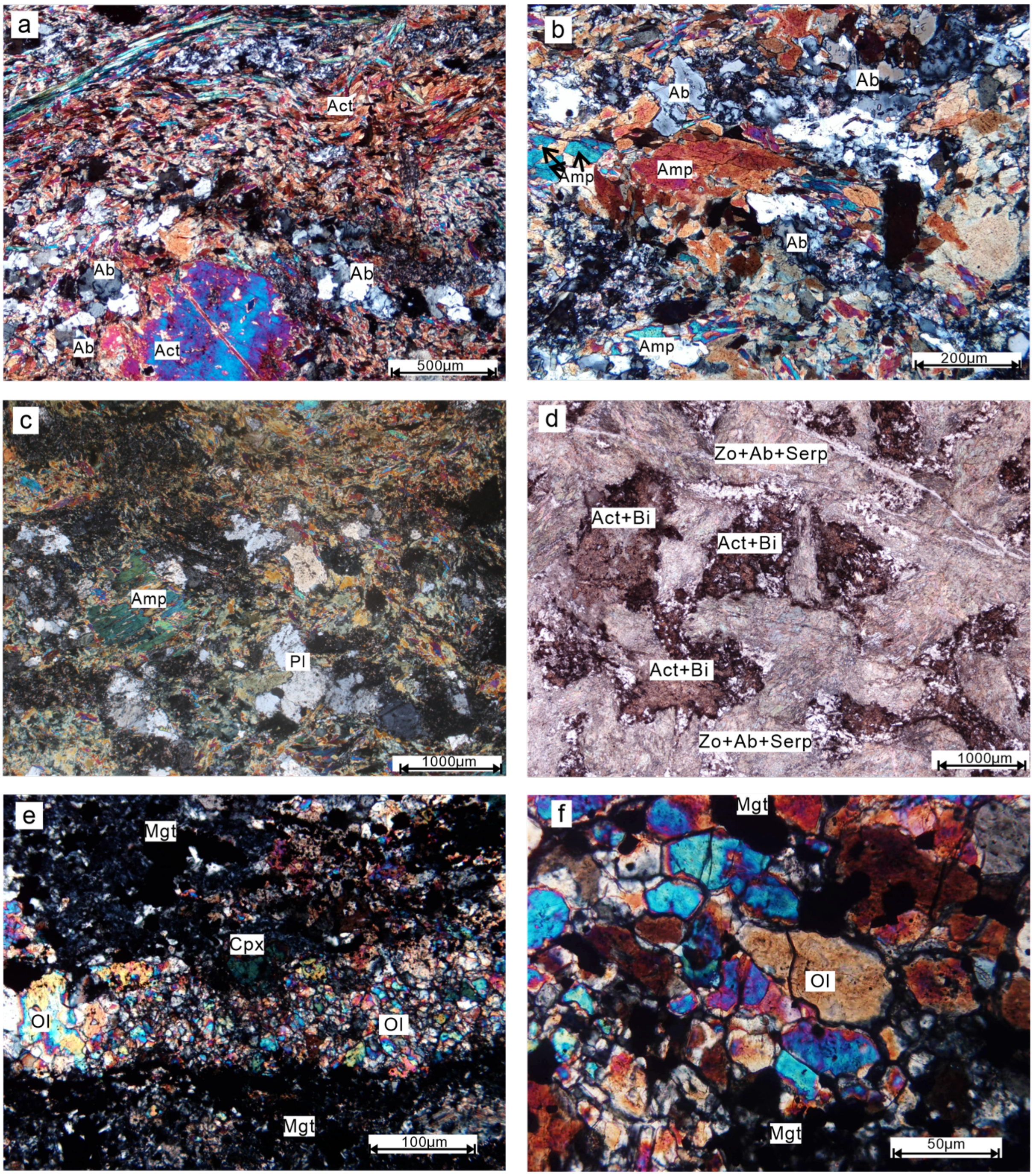

Figure 5. Photomicrographs of different samples from the Zeluo mafic-ultramafic rocks, Sichuan Province, SW China: (a) Strongly deformed metamorphic gabbro. (b, c) Undeformed metamorphic gabbro showing its mineral distribution. (d) Undeformed metamorphic gabbro showing its mineral distribution, plagioclase crystals are replaced by zoisite, albite and sericite, while most pyroxene crystals are altered/occupied by actinolite and a small amount of biotite. (e, f) Fine-grain dunites with euhedral magnesiochromite and strongly serpentinized olivine,

most magnesiochromite (Spl) is altered to magnetite (Mgt). Ab = albite; Act = actinolite; Amp = amphibole; Bi = biotite; Cpx = clinopyroxene; Ol = olivine; Pl = plagioclase; Serp = serpentine; Spl = magnesiochromite; Zo = Zoisite.

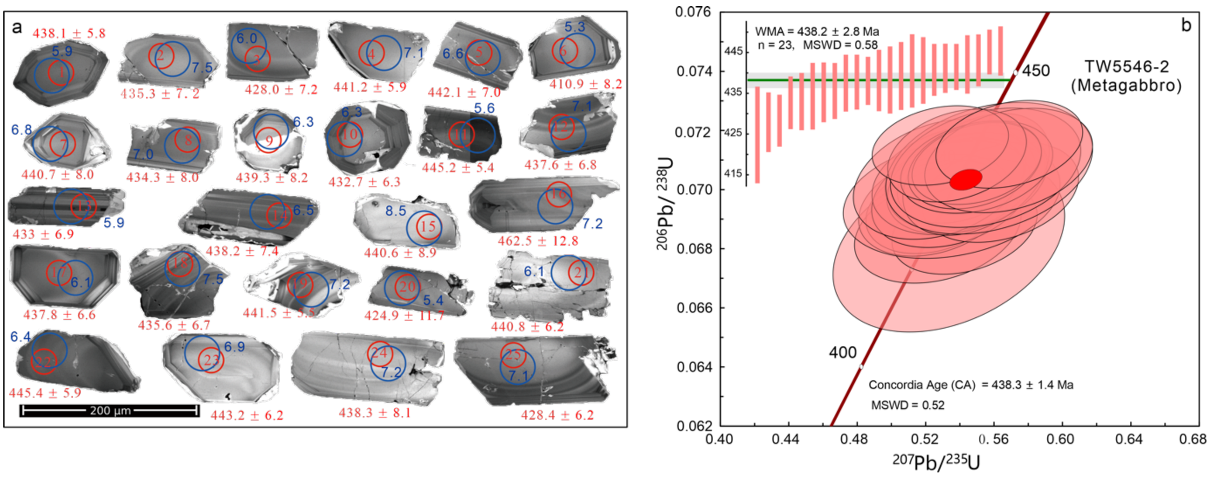

Figure 6. (a) CL image of zircon crystals from the Zeluo metamorphosed gabbro (TW5546-2) and (b) a U-Pb concordant diagram. In Figure a, the red circles reflect the analytical spots for U-Pb dating with associated ages; blue circles reflect Lu-Hf analytical spots with corresponding $\varepsilon_{Hf}(t)$ values.

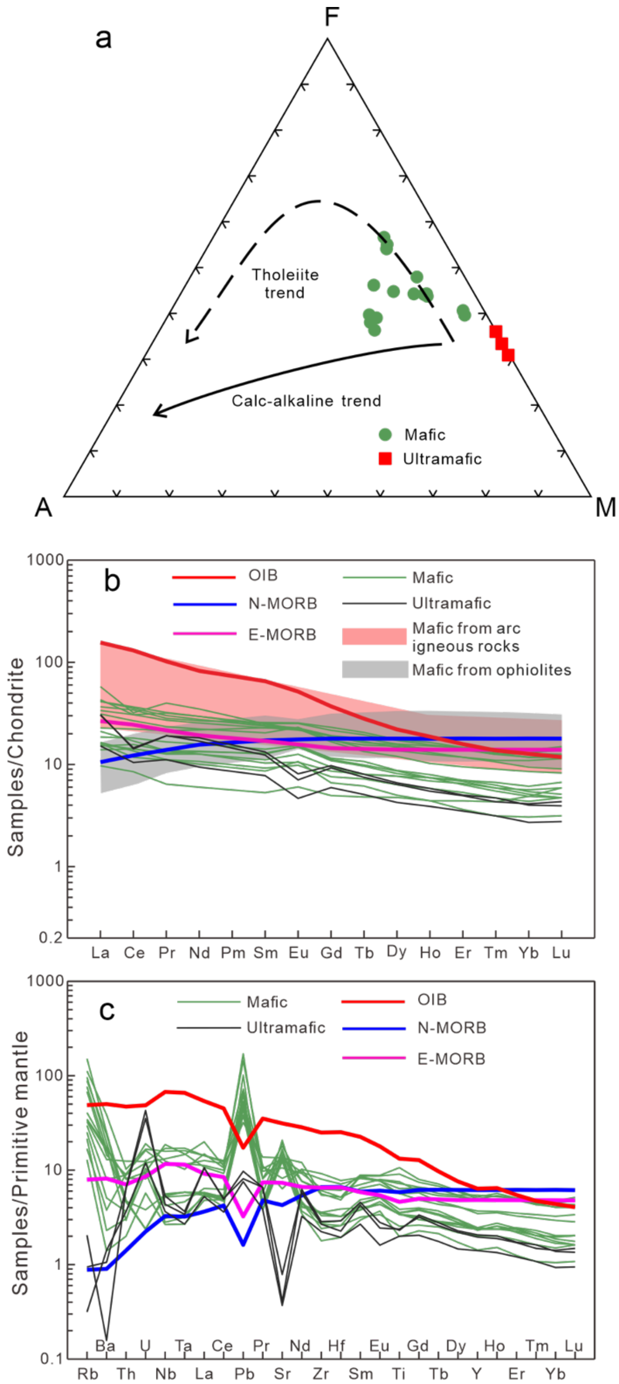

Figure 7. (a) AFM, a chemical classification for the common volcanic rocks, A = Na_2O+K_2O, F = FeO+Fe_2O_3, M = Mg. (b) Chondrite-normalized REE diagrams. The gray area indicates mafic rock data from an Early Paleozoic spreading ridge, from the Longmucuo-Shuanghu-Changning-Menglian suture zone (Hu et al., 2009; Zhai et al., 2010; Hu et al., 2014; Zhai et al., 2016), and the pink area indicates mafic rock data recording an Early Paleozoic subduction event in the same suture zone, with arc-like characteristics (Mao et al., 2012; Zhang et al., 2014;

Wu et al., 2016b; Wang et al., 2019a; Liu et al., 2021). (c) Primitive mantle-normalized multi-element diagrams for the Zeluo mafic-ultramafic rocks, Sichuan Province, SW China. Normalizing values are from McDonough and Sun (1995).

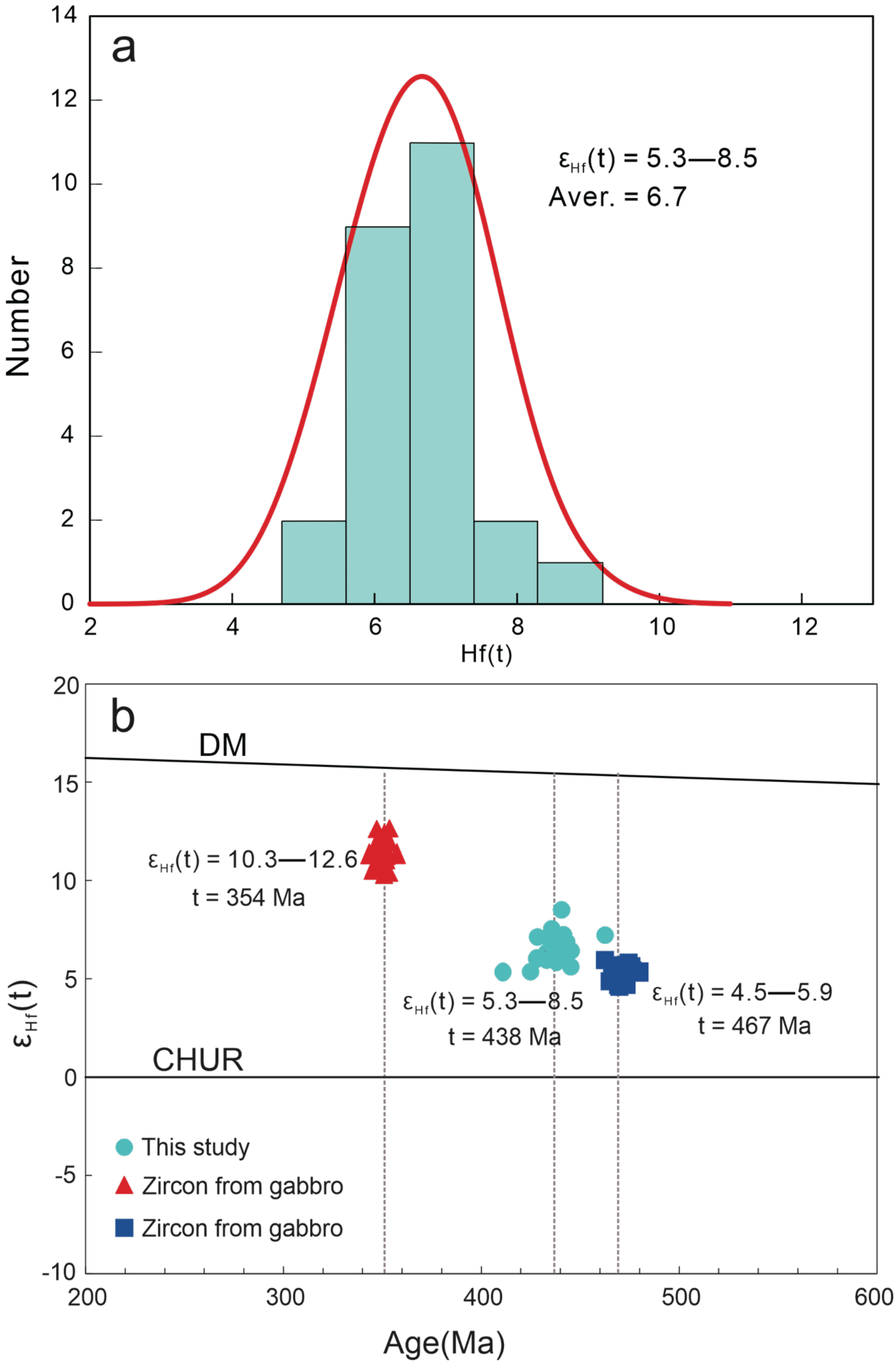

Figure 8. (a) Frequency distribution histogram for the zircon Hf isotope data. (b) Zircon $\varepsilon_{Hf}(t)$

versus age diagram. The zircon Hf isotope data (mafic rocks) is from Zhai et al. (2010) (blue square) and Wang et al. (2012) (red triangle). DM = depleted mantle evolution line, CHUR = chondrite average reservoir.

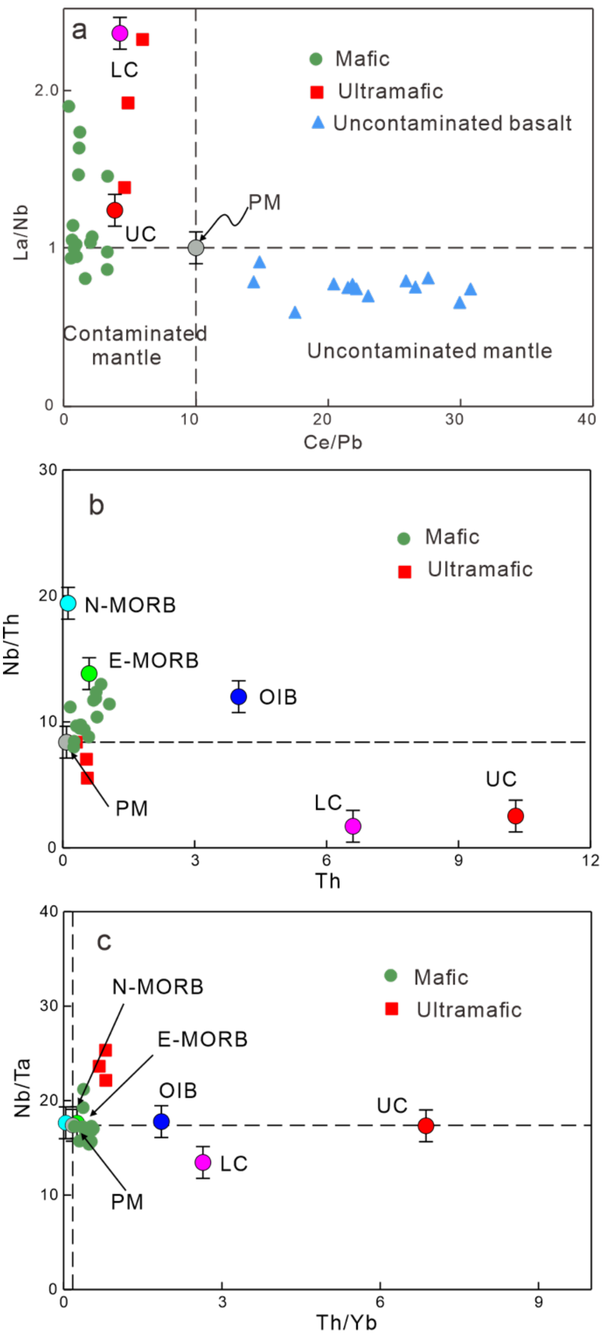

Figure 9. Geochemical variation diagrams for Zeluo mafic-ultramafic intrusions in Heni area, eastern Tibet, China, , (a) La/Nb vs. Ce/Pb. (b) Nb/Th vs. Th. (c) Nb/Ta vs. Th/Yb. Uncontaminated basalts data from Rooney et al. (2007). Values of N-MORB, E-MORB, and

OIB are from Sun and McDonough (1989). Values of primitive mantle (PM) are form McDonough and Sun (1995). Values for the upper crust (UC) and lower crust (LC) are from Wedepohl (1995).

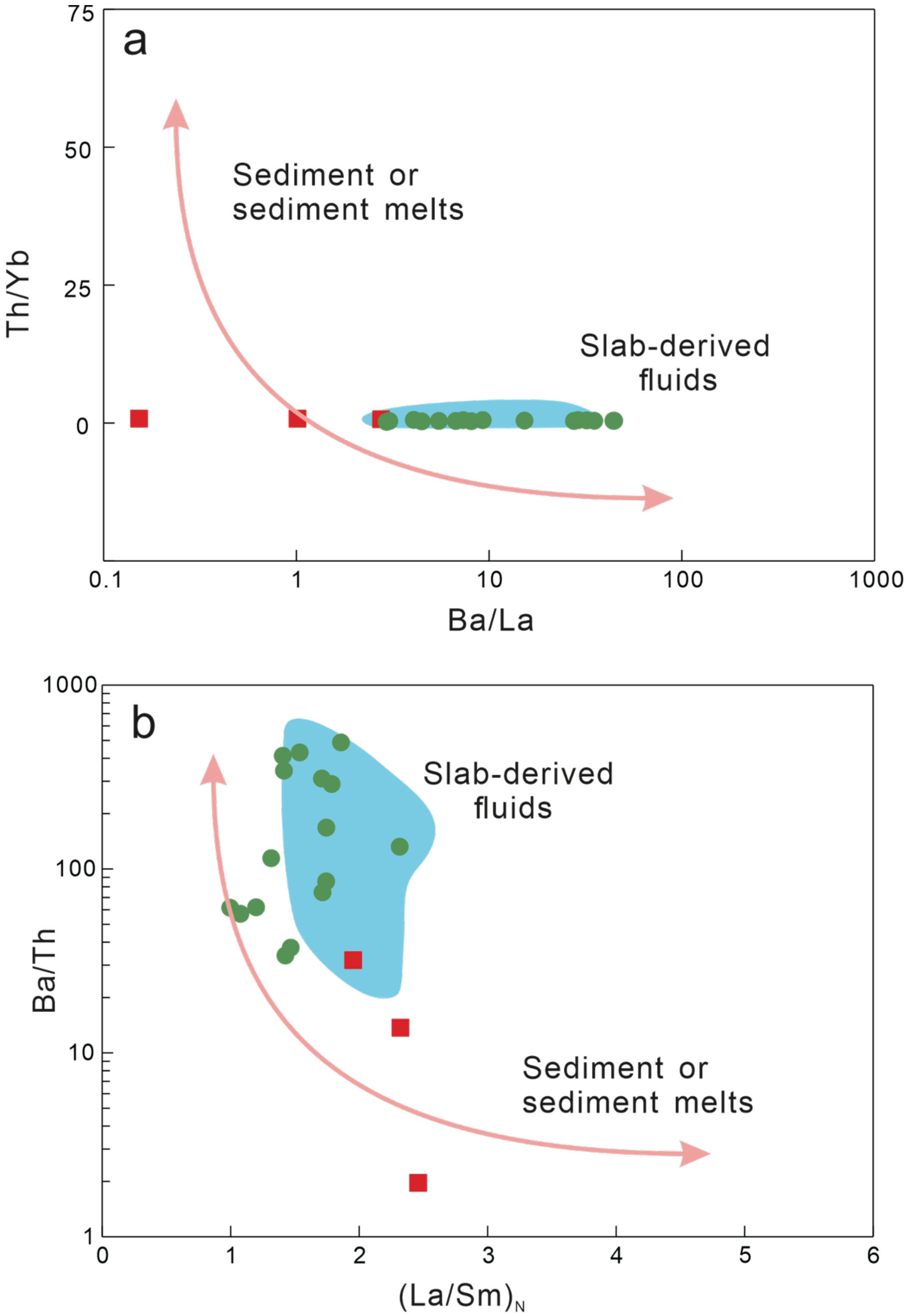

Figure 10. Geochemical plots for the Zeluo mafic-ultramafic rocks from Heni area, eastern Tibet, China: (a) Th/Yb vs. Ba/La. (b) Ba/Th vs. $(La/Sm)_N$.

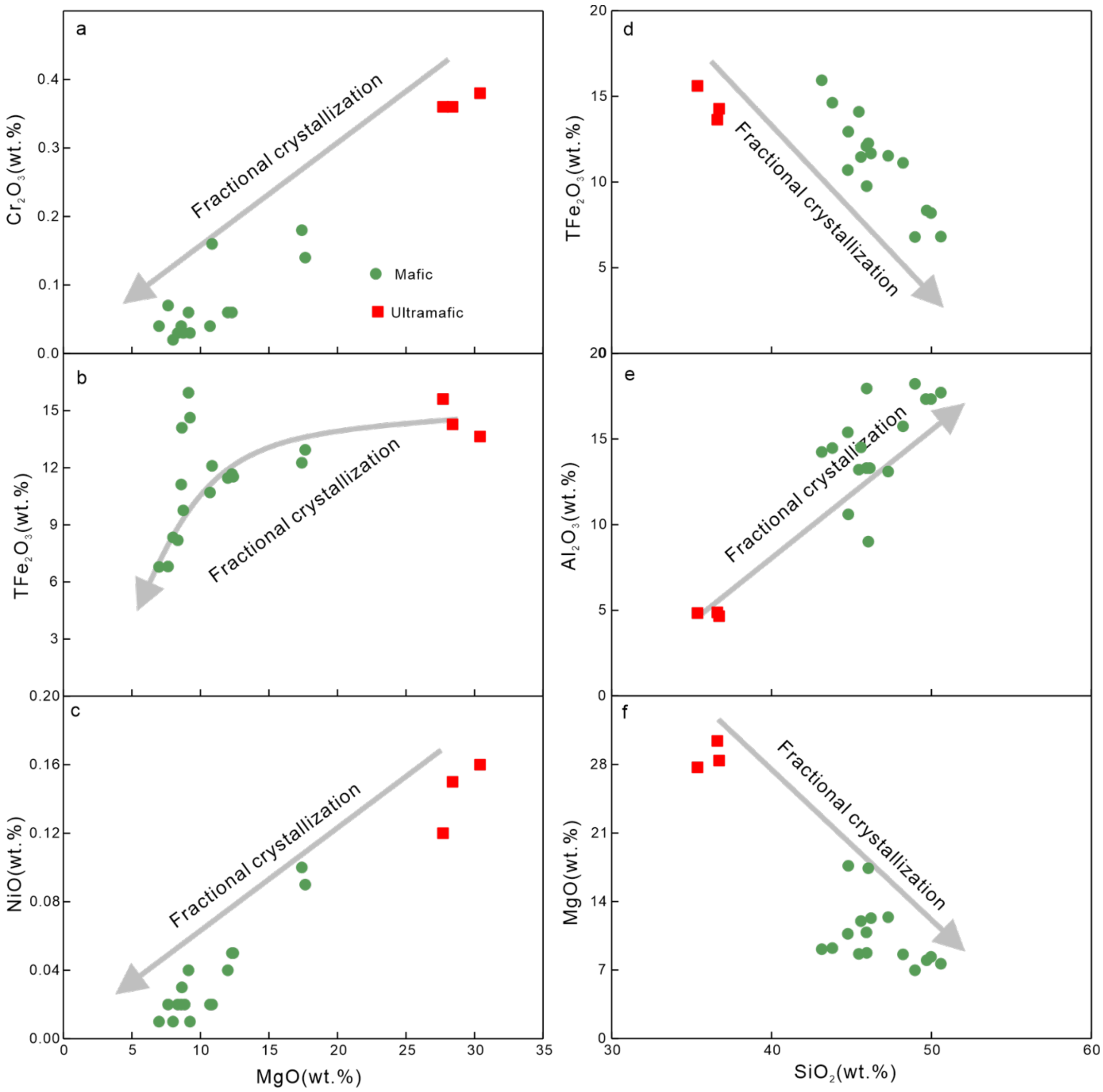

Figure 11. (a-f) Harker diagrams for Zeluo mafic-ultramafic samples, Eastern Tibet, China.

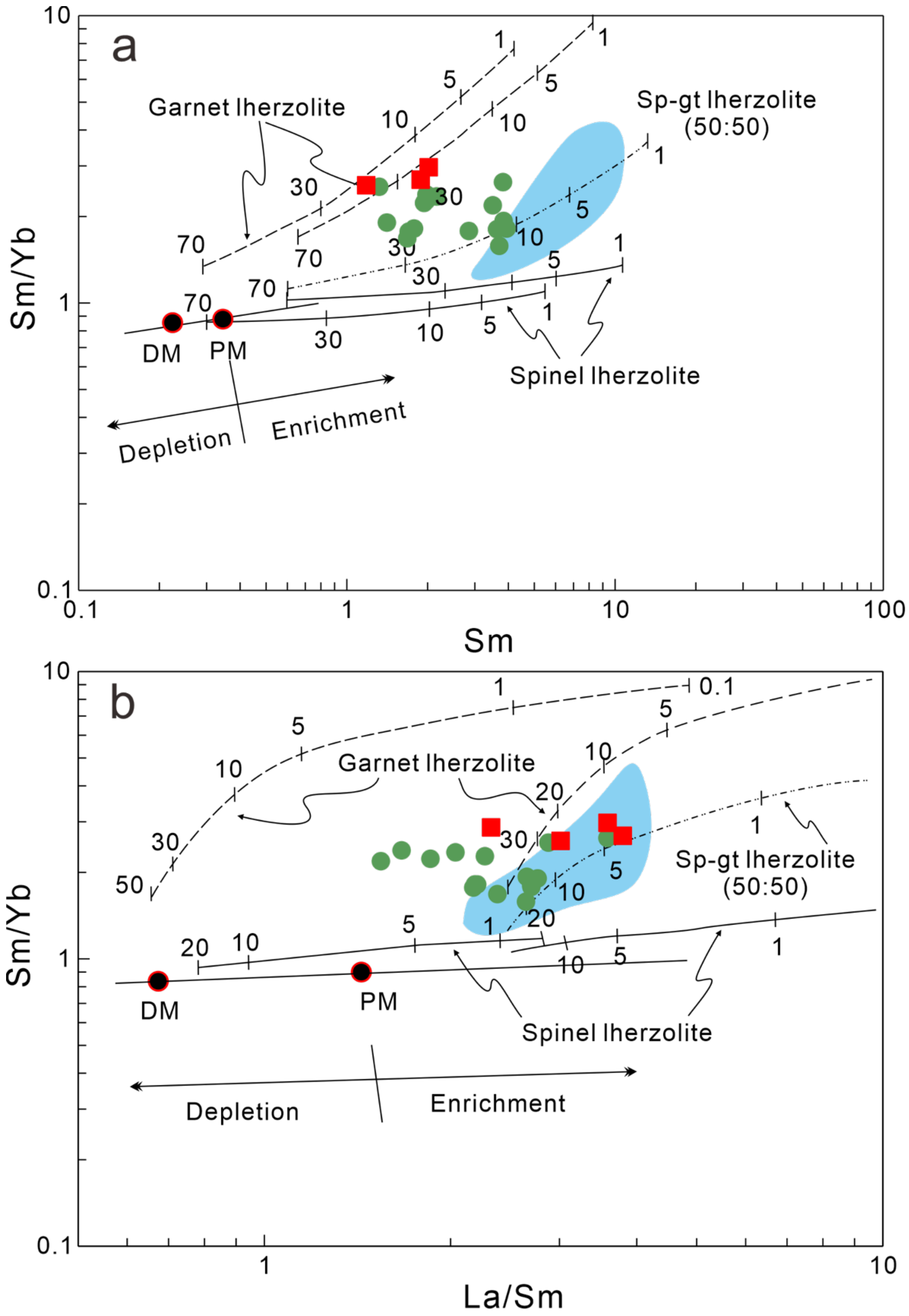

Figure 12. Geochemical plots for the Zeluo mafic-ultramafic rocks fromHeni area, eastern Tibet, China: (a) Sm/Yb vs. Sm. (b) Sm/Yb vs. La/Sm. Depleted mantle (DM) data from McKenzie and O'Nions (1991), primitive mantle (PM) data from McDonough and Sun (1995). Melting curves for spinel lherzolite (Ol_{53} + Opx_{27} + Cpx_{17} + Sp_{03}) and garnet peridotite (Ol_{60} +

$Opx_{20} + Cpx_{10} + Gt_{10}$) are from Aldanmaz et al. (2000), numbers along the lines represent the degree of partial melting; green circles for mafic rocks, red squares for ultramafic rocks. Blue area in (a-d) indicate data from Early Paleozoic subduction-derived mafic rocks from the Longmucuo-Shuanghu-Changning-Menglian suture zone (Mao et al., 2012; Zhang et al., 2014; Wu et al., 2016b; Wang et al., 2019a).

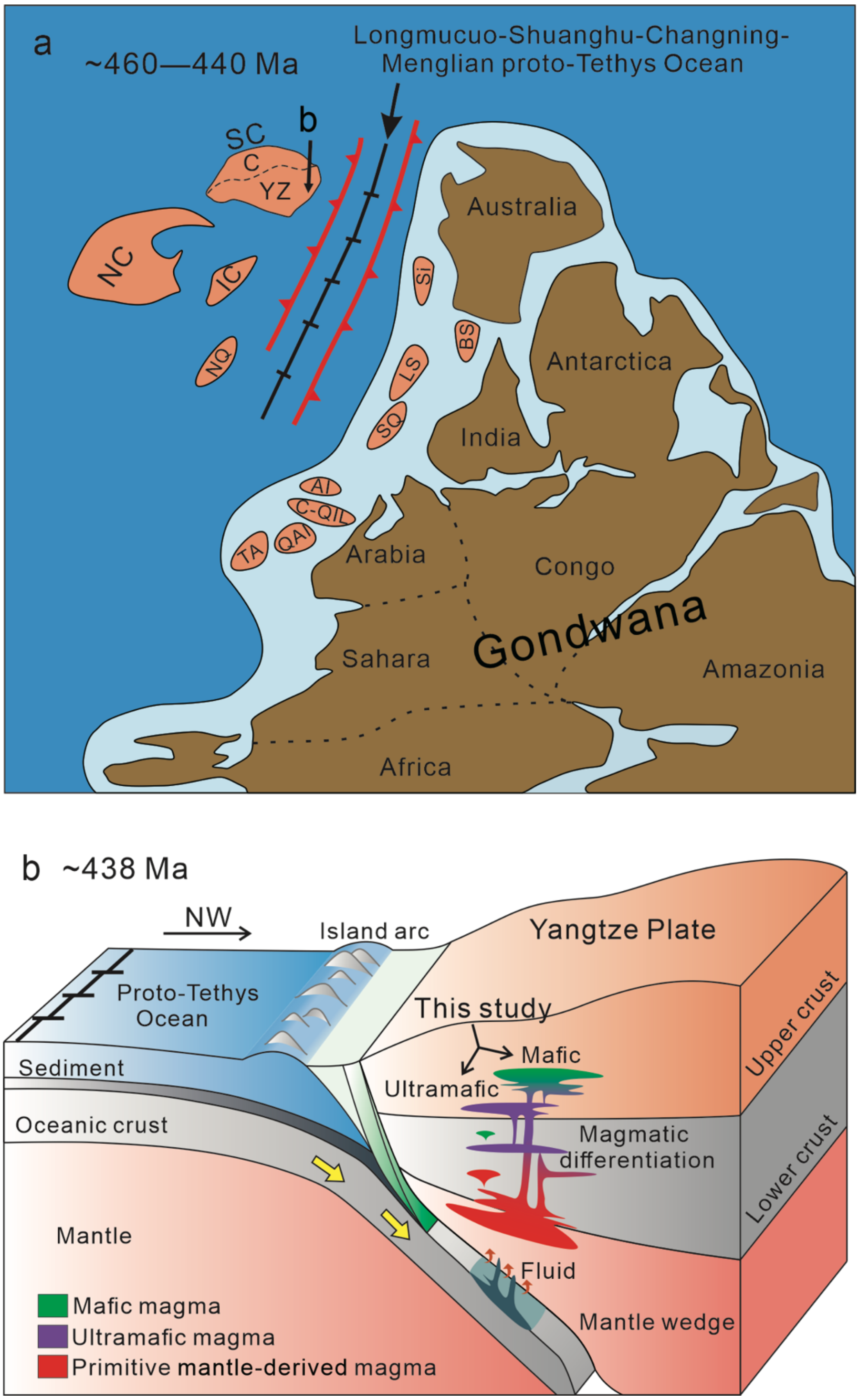

Figure 13. Schematic illustrates a model for the generation and evolution of the Zeluo pluton, eastern Tibet, China, (a) Schematic tectonic cartoons showing the Early Paleozoic tectonic evolution of the northern margin of Gondwana (Huang et al., 2018; Zhao et al., 2018; Liu et al., 2021). SQ = South Qiangtang, LS = Lhasa, BS = Baoshan, Si = Sibumasu, NQ = North Qiangtang, IC = Indochina, YZ = Yangtze, C = Cathaysian, TA = Tarim, QAI = Qaidam, C-QIL= Central-Qilian, AL = Alex, SC = South China, NC = North China. (b) A sketch map only showing the northwestward subduction of the Longmucuo-Shuanghu-Changning-Menglian Proto-Tethyan Ocean, forming the Zeluo mafic-ultramafic rock intrusion on the western margin of the Yangtze plate.

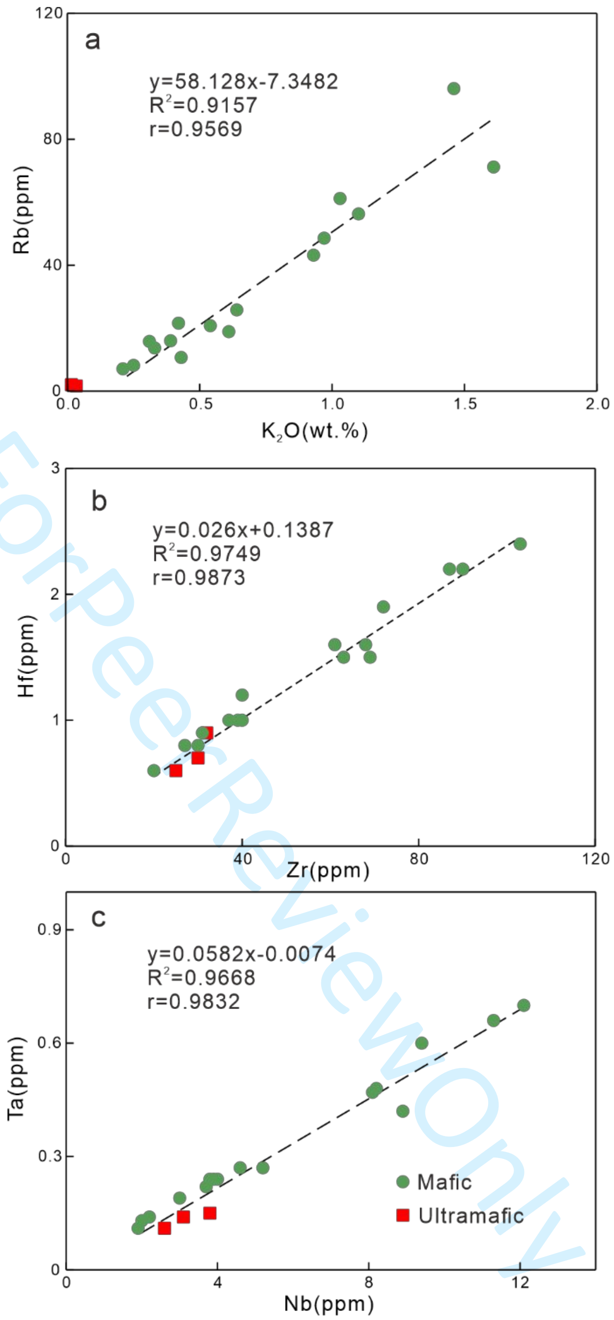

Figure S1. Alteration assessment plots for the mafic-untramafic rocks from Zeluo, Sichuan Province, SW China, (a) K_2O (wt.%) vs. Rb (ppm), (b) Zr (ppm) vs. Hf (ppm), and (c) Ta (ppm) vs. Nd (ppm).

Supp. Table 1: LA-ICP-MS U-Pb data of zircons from the metamorphic gabbro (TW5546-2) in Zeluo, Eastern Tibet, China

Analysis	Pb^{Total}	^{232}Th	^{238}U	Pb^{C}	Ratio									Age (Ma)								Con.
Spots	ppm	ppm	ppm	ppm	$^{207}Pb/^{206}Pb$	1σ	$^{207}Pb/^{235}U$	1σ	$^{206}Pb/^{238}U$	1σ	$^{208}Pb/^{232}Th$	1σ	$^{238}U/^{232}Th$	$^{207}Pb/^{206}Pb$	1σ	$^{207}Pb/^{235}U$	1σ	$^{206}Pb/^{238}U$	1σ	$^{208}Pb/^{232}Th$	1σ	
TW5546-2-1	203	686	550	61.1	0.0556	0.0026	0.5409	0.0244	0.0703	0.0010	0.0216	0.0006	0.9232	435	136	439	16	438	6	432	11	99%
TW5546-2-2	87	283	306	43.8	0.0557	0.0036	0.5353	0.0307	0.0699	0.0012	0.0213	0.0007	1.2331	439	144	435	20	435	7	425	13	99%
TW5546-2-3	118	395	410	41.5	0.0556	0.0035	0.5276	0.0322	0.0686	0.0012	0.0210	0.0007	1.1834	435	143	430	21	428	7	421	14	99%
TW5546-2-4	119	408	404	49.3	0.0569	0.0029	0.5493	0.0257	0.0708	0.0010	0.0202	0.0005	1.1240	500	113	445	17	441	6	405	9	99%
TW5546-2-5	92	288	304	37.4	0.0582	0.0035	0.5690	0.0324	0.0710	0.0012	0.0222	0.0006	1.1975	600	133	457	21	442	7	444	12	96%
TW5546-2-6	113	381	396	46.2	0.0595	0.0047	0.5454	0.0443	0.0658	0.0014	0.0209	0.0008	1.1718	583	170	442	29	411	8	417	17	92%
TW5546-2-7	137	443	429	59.4	0.0554	0.0042	0.5555	0.0368	0.0707	0.0013	0.0218	0.0008	1.0673	428	166	449	24	441	8	436	16	98%
TW5546-2-8	187	656	542	59.0	0.0559	0.0046	0.5357	0.0419	0.0697	0.0013	0.0206	0.0007	0.8932	456	183	436	28	434	8	412	14	99%
TW5546-2-9	71	226	252	52.0	0.0518	0.0046	0.5500	0.0283	0.0705	0.0014	0.0226	0.0007	1.2584	276	204	445	19	439	8	451	15	98%
TW5546-2-10	135	447	439	40.9	0.0551	0.0029	0.5265	0.0271	0.0694	0.0010	0.0215	0.0005	1.0283	417	117	429	18	433	6	430	10	99%
TW5546-2-11	237	821	603	54.5	0.0532	0.0027	0.5290	0.0263	0.0715	0.0009	0.0218	0.0005	0.7959	345	119	431	17	445	5	435	11	96%
TW5546-2-12	95	314	328	65.9	0.0543	0.0032	0.5414	0.0288	0.0702	0.0011	0.0211	0.0006	1.0530	383	133	439	19	438	7	422	12	99%
TW5546-2-13	103	359	335	50.9	0.0524	0.0032	0.5257	0.0294	0.0695	0.0011	0.0205	0.0006	0.9384	306	136	429	20	433	7	411	11	99%
TW5546-2-14	171	585	518	33.8	0.0565	0.0039	0.5403	0.0339	0.0703	0.0012	0.0213	0.0005	0.9072	478	147	439	22	438	7	426	10	99%
TW5546-2-15	82	263	289	51.9	0.0548	0.0044	0.5576	0.0400	0.0707	0.0015	0.0220	0.0010	1.1352	406	181	450	26	441	9	439	19	97%
TW5546-2-16	115	391	365	59.1	0.0531	0.0049	0.5470	0.0498	0.0744	0.0021	0.0209	0.0010	0.9760	332	211	443	33	463	13	418	20	95%
TW5546-2-17	91	307	327	35.6	0.0550	0.0033	0.5445	0.0304	0.0703	0.0011	0.0213	0.0006	1.1302	413	133	441	20	438	7	425	13	99%
TW5546-2-18	53.1	158	236	56.4	0.0542	0.0034	0.5643	0.0301	0.0699	0.0011	0.0228	0.0009	1.6226	389	143	454	20	436	7	456	17	95%
TW5546-2-19	247	883	571	68.2	0.0559	0.0029	0.5503	0.0250	0.0709	0.0009	0.0217	0.0005	0.7121	450	117	445	16	442	6	435	11	99%
TW5546-2-20	71	232	257	34.7	0.0528	0.0058	0.5340	0.0447	0.0681	0.0019	0.0221	0.0010	1.1976	320	249	434	30	425	12	442	19	97%
TW5546-2-21	84	275	301	63.2	0.0548	0.0031	0.5503	0.0294	0.0708	0.0010	0.0219	0.0007	1.1805	467	128	445	19	441	6	438	14	99%
TW5546-2-22	108	345	354	50.9	0.0571	0.0030	0.5694	0.0283	0.0715	0.0010	0.0227	0.0006	1.1045	494	116	458	18	445	6	454	12	97%
TW5546-2-23	152	531	462	64.7	0.0547	0.0028	0.5389	0.0268	0.0712	0.0010	0.0209	0.0005	0.9462	467	113	438	18	443	6	417	11	98%
TW5546-2-24	103	342	340	36.0	0.0544	0.0035	0.5286	0.0333	0.0704	0.0013	0.0220	0.0007	1.0628	387	144	431	22	438	8	439	14	98%
TW5546-2-25	135	459	445	52.4	0.0575	0.0031	0.5432	0.0281	0.0687	0.0010	0.0215	0.0006	1.0392	509	120	441	18	428	6	429	11	97%

Pb^{C}: Common Pb

Supp. Table 2: Chemical compositions for Olivine from the ultramafic rocks in Zeluo, Eastern Tibet, China

Olivine	0003-4	0003-5	0003-6	0003-7	0003-17	0004-1	0004-2	0004-3	0004-4	0004-5	0004-6	0004-7	0004-8	0004-9	0004-10	0004-11	0004-12	0004-13	0004-14	0004-15	0004-16	0004-18	0004-19	0004-20
SiO_2	42.22	42.23	42.2	42.42	41.31	42.05	41.82	41.97	42.39	42.02	41.91	42.1	42.18	41.73	42.18	42.6	42.35	42.17	42.22	42.29	42.25	42.31	41.89	42.56
TiO_2					0.02	0.01	0.03										0.01	0.01	0.01		0.03		0.01	
Al_2O_3				0.01	0.01			0.02			0.02		0.01	0.01								0.01	0.02	
Cr_2O_3	0.03	0.04	0.05	0.01	0.01	0.04	0.04	0.05	0.05		0.11	0.01	0.02	0.01		0.07	0.05	0.03		0.07	0.05			0.02
FeO	6.75	6.8	6.95	6.62	6.46	6.47	6.92	6.57	6.28	6.52	6.73	6.14	6.35	6.53	6.1	6.57	6.52	6.88	7.01	6.19	6.78	6.3	6.39	6.34
MnO	0.32	0.35	0.3	0.33	0.27	0.32	0.39	0.33	0.32	0.3	0.36	0.32	0.31	0.28	0.32	0.32	0.35	0.34	0.32	0.36	0.31	0.34	0.35	0.32
MgO	51.49	51.8	51.33	51.93	50.48	51.35	51.63	51.87	51.56	51.87	51.58	51.86	51.32	51.62	52.21	51.74	51.26	51.8	52.26	52.16	52.38	51.94	51.68	51.15
NiO	0.04	0.029	0.082	0.072	0	0.04	0.08	0.014	0.048	0.079	0.049	0.07	0.101	0.075	0.021	0.1	0.035	0.037	0.095	0.09	0.081	0.079	0.003	0.066
CaO	0.21	0.03	0.04	0.12	1.25	0.11	0.09	0.17	0.14	0.11	0.05	0.15	0.06	0.12	0.15	0.04	0.20	0.07	0.15	0.06	0.05	0.05	0.09	0.22
Total	101.077	101.29	100.954	101.511	99.81	100.381	101.001	100.991	100.797	100.909	100.801	100.656	100.353	100.393	100.987	101.455	100.774	101.331	102.063	101.233	101.957	101.042	100.432	100.694
Fo	92.84	92.81	92.65	93.01	93.04	93.09	92.64	93.05	93.30	93.13	92.84	93.46	93.21	93.11	93.54	93.04	93.00	92.74	92.70	93.41	92.94	93.30	93.18	93.19

Supp. Table 3: Chemical compositions for Pyroxene from the mafic-ultramafic rocks in Zeluo, Eastern Tibet, China

Pyro	0001-1	0001-3	0002-2	0002-3	0003-1	0003-2	0003-3	0003-8	0003-9	0003-11	0003-12	0003-13	0003-14	0003-16	0003-18	0003-20
SiO_2	56.813	52.401	55.374	53.606	55.478	54.194	54.604	55.621	55.244	55.75	55.639	56.229	56.21	54.832	55.273	54.834
TiO_2	0	0.471	0.127	0.356	0.176	0.272	0.24	0.212	0.142	0.05	0.018	0.093	0.038	0.170	0.212	0.104
Al_2O	0.259	3.533	0.877	2.585	0.938	1.629	1.44	0.896	1.504	0.872	0.540	0.314	0.201	1.580	1.076	0.864
Cr_2O	0.135	0.023	0.181	0.037	0.102	0.037	0.117	0.038	0.141	0.09	0.094	0.137	0.113	0.052	0.111	0.005
FeO	2.071	2.419	2.131	2.241	2.795	2.547	2.675	2.440	2.098	2.454	2.190	2.481	2.184	2.591	2.212	2.387
MnO	0.040	0.019	0.036	0.018	0.031	0.069	0.030	0.042	0.014	0.055	0.061	0.032	0.076	0.012	0.017	0.044
MgO	17.292	16.038	17.041	16.546	16.841	16.588	16.632	16.798	17.207	16.938	17.112	16.884	17.087	17.144	16.927	16.922
CaO	26.102	26.034	25.937	25.842	25.733	25.901	25.923	26.068	25.931	25.903	25.743	25.78	25.657	25.968	25.902	25.921
Na_2O	0.023	0	0	0	0.030	0.013	0.021	0.027	0	0.025	0.024	0.011	0.013	0.018	0.036	0.005
K_2O	0	0	0.002	0	0.010	0.003	0.016	0.007	0	0.005	0.003	0	0.004	0	0.002	0.011
NiO	0.001	0.020	0	0.072	0.038	0.017	0.003	0.018	0.054	0.027	0.008	0	0	0.030	0	0
Total	102.736	100.958	101.706	101.303	102.172	101.27	101.701	102.167	102.335	102.169	101.432	101.961	101.583	102.397	101.768	101.097
Wo	50.34	51.79	50.52	51.03	50.03	50.74	50.62	50.68	50.33	50.30	50.13	50.30	50.09	50.05	50.52	50.45
En	46.40	44.41	46.18	45.48	45.56	45.22	45.18	45.44	46.47	45.78	46.37	45.82	46.42	45.96	45.94	45.82
Fs	3.19	3.80	3.30	3.49	4.30	4.00	4.13	3.77	3.20	3.81	3.43	3.84	3.46	3.91	3.40	3.69
Ac	0.07	0.00	0.00	0.00	0.11	0.04	0.07	0.11	0.00	0.11	0.07	0.04	0.04	0.07	0.14	0.04

Supp. Table 4: Major oxides (ωt%) and element (ppm) abundances for the mafic-ultramafic rocks in Zeluo, Eastern Tibet, China

Samples	D5533-2	D5533-3	HF5517-3	D5533-4	D5533-6	D5537	D5539-1	D5533-7	D5540-2	D5545-1	D5546-1	D5546-2	D5546-3	HF5517-1	HF5517-2	HF5517-4	HF5517-6	HF5517-8	HF5517-9	D5546-1	D5546-2	D5546-3	HF5517-1
Types	Ultramafic Rocks			Mafic Rocks																			
SiO_2	36.72	36.61	35.37	44.80	48.22	50.59	46.05	44.77	45.95	43.14	48.97	49.70	49.97	45.46	43.80	45.93	45.59	47.29	46.22	48.97	49.70	49.97	45.46
Al_2O_3	4.66	4.88	4.84	10.60	15.74	17.71	9.01	15.39	17.95	14.24	18.22	17.34	17.33	13.21	14.47	13.30	14.51	13.10	13.30	18.22	17.34	17.33	13.21
TFe_2O_3	14.28	13.64	15.61	12.94	11.12	6.81	12.26	10.70	9.76	15.94	6.79	8.34	8.19	14.10	14.63	12.10	11.46	11.53	11.67	6.79	8.34	8.19	14.10
MgO	28.40	30.40	27.70	17.65	8.60	7.64	17.40	10.70	8.75	9.13	6.98	8.00	8.35	8.65	9.24	10.85	12.00	12.40	12.30	6.98	8.00	8.35	8.65
CaO	7.08	5.25	6.88	8.11	9.36	10.80	10.15	12.45	10.45	9.87	11.70	8.68	9.32	12.10	10.60	14.00	11.20	11.45	11.35	11.70	8.68	9.32	12.10
Na_2O	0.10	0.11	0.01	0.96	3.83	3.87	1.08	1.85	2.32	1.48	2.62	3.57	3.42	2.25	2.75	1.65	2.11	2.18	2.06	2.62	3.57	3.42	2.25
K_2O	0.01	<0.01	0.01	0.31	0.54	0.42	0.21	0.93	0.97	1.61	1.46	1.10	1.03	0.61	0.43	0.64	0.39	0.25	0.33	1.46	1.10	1.03	0.61
MnO	0.33	0.31	0.34	0.25	0.18	0.14	0.22	0.20	0.23	0.30	0.14	0.16	0.16	0.31	0.35	0.31	0.22	0.20	0.21	0.14	0.16	0.16	0.31
TiO_2	0.50	0.45	0.53	1.46	1.41	0.55	0.76	1.24	1.26	1.51	0.72	0.72	0.73	2.16	2.45	0.45	0.91	0.81	0.79	0.72	0.72	0.73	2.16
P_2O_5	0.10	0.07	0.10	0.14	0.17	0.06	0.07	0.13	0.12	0.18	0.12	0.06	0.06	0.20	0.27	0.03	0.06	0.02	0.04	0.12	0.06	0.06	0.20
LOI	8.03	8.37	7.94	2.74	1.36	1.11	2.14	1.29	1.81	2.29	2.26	1.92	2.06	1.52	1.50	0.86	1.57	0.85	1.11	2.26	1.92	2.06	1.52
Total	92.18	91.72	91.39	97.22	99.17	98.59	97.21	98.36	97.76	97.40	97.72	97.67	98.56	99.05	98.99	99.26	98.45	99.23	98.27	97.72	97.67	98.56	99.05
FeO	4.10	4.03	4.60	10.55	8.44	5.36	9.54	8.27	7.76	12.65	5.14	6.56	6.42	10.90	11.25	9.18	8.78	9.00	9.02	5.14	6.56	6.42	10.90
$Mg^{\#}$	0.79	0.81	0.78	0.71	0.59	0.67	0.72	0.65	0.62	0.51	0.66	0.64	0.65	0.53	0.54	0.62	0.66	0.66	0.66	0.71	0.59	0.67	0.72
Rb	0.60	0.20	1.30	15.80	20.80	21.60	7.10	43.20	48.60	71.20	96.10	56.30	61.20	18.90	10.70	25.80	16.00	8.20	13.70	96.10	56.30	61.20	18.90
Ba	7.40	9.90	1.10	36.30	90.80	113.00	18.30	100.50	117.50	270.00	176.50	165.00	137.00	56.00	26.40	122.00	35.50	9.70	16.10	176.50	165.00	137.00	56.00
Th	0.54	0.31	0.56	0.59	1.06	0.39	0.49	0.76	0.70	0.87	0.41	0.40	0.40	0.75	0.78	0.25	0.31	0.17	0.26	0.41	0.40	0.40	0.75
Ti	0.30	0.26	0.309	0.793	0.828	0.331	0.458	0.729	0.739	0.938	0.439	0.443	0.444	1.18	1.38	0.257	0.501	0.462	0.456	0.439	0.443	0.444	1.18
U	0.74	0.25	0.90	0.17	0.26	0.05	0.28	0.25	0.17	0.35	0.05	0.08	0.05	0.40	0.34	0.27	0.22	0.12	0.20	0.05	0.08	0.05	0.40
Sc	14.80	14.10	14.80	25.40	35.30	30.50	21.30	41.00	29.70	29.90	34.00	29.40	29.50	40.10	44.50	31.10	43.80	48.90	45.50	34.00	29.40	29.50	40.10
V	145	135	153	284	250	151	138	258	220	221	154	132	137	576	659	131	266	273	265	154	132	137	576
Cr	2972	3039	3060	1113	292	526	1287	263	200	406	240	144	172	120	190	1410	450	550	490	240	144	172	120
Co	123.5	115.5	119	73.40	41.90	33.30	71.90	45.00	41.10	39.90	36.80	41.20	41.60	38.60	44.30	34.10	54.00	55.40	58.50	36.80	41.20	41.60	38.60
Ni	1180	1260	1090	754	97.1	117	774	141	79.1	213	62.2	60.4	67.9	82	85.4	241	372	339	326	62.2	60.4	67.9	82
Pb	1.80	1.40	1.50	6.70	13.30	13.00	3.30	5.90	31.50	6.80	11.60	8.90	9.50	26.70	9.70	18.70	9.90	7.10	8.20	11.60	8.90	9.50	26.70
Zn	493	594	555	101	78	71	110	101	77	144	60	77	76	192	98	138	85	74	82	60	77	76	192

Ga	9.40	8.30	9.10	18.60	17.10	14.30	15.10	19.00	19.90	19.30	15.90	15.10	13.60	19.30	20.50	14.10	15.70	13.50	14.10	15.90	15.10	13.60	19.30
Ta	0.15	0.11	0.14	0.27	0.70	0.22	0.27	0.60	0.48	0.66	0.24	0.24	0.24	0.42	0.47	0.13	0.19	0.11	0.14	0.24	0.24	0.24	0.42
Nb	3.80	2.60	3.10	5.20	12.10	3.70	4.60	9.40	8.20	11.30	4.00	3.90	3.80	8.90	8.10	2.00	3.00	1.90	2.20	4.00	3.90	3.80	8.90
Sr	8.60	7.80	16.60	47.10	279.00	308.00	44.90	284.00	379.00	134.00	438.00	268.00	283.00	173.00	223.00	260.00	412.00	351.00	333.00	438.00	268.00	283.00	173.00
Zr	32.00	25.00	30.00	87.00	90.00	30.00	69.00	63.00	68.00	103.00	39.00	40.00	40.00	61.00	72.00	20.00	37.00	27.00	31.00	39.00	40.00	40.00	61.00
Hf	0.90	0.60	0.70	2.20	2.20	0.80	1.50	1.50	1.60	2.40	1.00	1.00	1.20	1.60	1.90	0.60	1.00	0.80	0.90	1.00	1.00	1.20	1.60
Y	9.40	6.40	8.90	20.00	22.00	9.20	10.50	15.80	16.80	24.70	11.20	10.80	10.80	22.60	23.60	6.50	11.20	10.50	10.60	11.20	10.80	10.80	22.60
La	7.30	3.60	7.20	5.40	9.80	3.90	4.50	13.70	7.70	9.80	4.00	3.70	3.90	10.20	8.70	3.80	4.40	3.30	3.60	4.00	3.70	3.90	10.20
Ce	8.70	6.40	8.90	13.60	21.70	8.30	10.90	19.60	17.70	22.40	9.20	8.70	8.90	18.80	20.90	7.20	11.10	8.70	9.60	9.20	8.70	8.90	18.80
Pr	1.81	1.06	1.82	2.04	2.86	1.06	1.49	3.79	2.25	3.07	1.20	1.20	1.20	3.02	2.69	1.05	1.58	1.23	1.30	1.20	1.20	1.20	3.02
Nd	8.50	4.40	7.90	10.20	12.90	5.00	7.10	16.30	10.30	13.80	5.60	5.90	5.50	13.80	12.50	4.70	7.40	6.20	6.30	5.60	5.90	5.50	13.80
Sm	2.03	1.19	1.89	3.50	3.63	1.41	1.98	3.82	2.85	3.70	1.68	1.70	1.78	3.84	3.94	1.32	2.16	1.98	1.94	1.68	1.70	1.78	3.84
Eu	0.47	0.27	0.41	1.26	1.29	0.57	0.78	1.29	1.19	1.32	0.78	0.73	0.73	1.46	1.48	0.62	0.89	0.86	0.86	0.78	0.73	0.73	1.46
Gd	2.00	1.22	1.90	3.91	3.87	1.56	2.05	3.43	2.89	3.94	1.89	1.94	1.79	4.44	4.75	1.36	2.37	2.30	2.24	1.89	1.94	1.79	4.44
Tb	0.30	0.19	0.28	0.63	0.61	0.27	0.33	0.50	0.47	0.67	0.31	0.30	0.30	0.73	0.77	0.23	0.40	0.37	0.36	0.31	0.30	0.30	0.73
Dy	1.68	1.08	1.62	3.74	3.99	1.61	1.98	3.05	3.01	4.03	2.01	1.95	1.85	4.36	4.45	1.27	2.22	2.19	2.07	2.01	1.95	1.85	4.36
Ho	0.33	0.22	0.31	0.74	0.79	0.33	0.39	0.58	0.60	0.86	0.39	0.39	0.39	0.88	0.93	0.25	0.45	0.42	0.42	0.39	0.39	0.39	0.88
Er	0.83	0.58	0.82	1.95	2.36	0.88	1.02	1.57	1.68	2.42	1.18	1.08	1.14	2.41	2.43	0.60	1.16	1.05	1.13	1.18	1.08	1.14	2.41
Tm	0.12	0.08	0.11	0.27	0.32	0.12	0.14	0.23	0.25	0.36	0.17	0.15	0.15	0.33	0.35	0.08	0.16	0.14	0.15	0.17	0.15	0.15	0.33
Yb	0.68	0.46	0.70	1.60	2.01	0.74	0.87	1.45	1.60	2.34	1.00	0.96	0.98	1.99	2.17	0.52	0.92	0.83	0.87	1.00	0.96	0.98	1.99
Lu	0.10	0.07	0.11	0.23	0.30	0.12	0.13	0.21	0.25	0.38	0.15	0.15	0.15	0.30	0.32	0.08	0.13	0.12	0.12	0.15	0.15	0.15	0.30
ΣREE	34.85	20.82	33.97	49.07	66.43	25.87	33.66	69.52	52.74	69.09	29.56	28.85	28.76	66.56	66.38	23.08	35.34	29.69	30.96	29.56	28.85	28.76	66.56
LREE	28.81	16.92	28.12	36.00	52.18	20.24	26.75	58.50	41.99	54.09	22.46	21.93	22.01	51.12	50.21	18.69	27.53	22.27	23.60	22.46	21.93	22.01	51.12
HREE	6.04	3.90	5.85	13.07	14.25	5.63	6.91	11.02	10.75	15.00	7.10	6.92	6.75	15.44	16.17	4.39	7.81	7.42	7.36	7.10	6.92	6.75	15.44
LREE/HREE	4.77	4.34	4.81	2.75	3.66	3.60	3.87	5.31	3.91	3.61	3.16	3.17	3.26	3.31	3.11	4.26	3.52	3.00	3.21	3.16	3.17	3.26	3.31
La_N/Yb_N	7.70	5.61	7.38	2.42	3.50	3.78	3.71	6.78	3.45	3.00	2.87	2.76	2.85	3.68	2.88	5.24	3.43	2.85	2.97	2.87	2.76	2.85	3.68

Supp. Table 5: Zircon in-situ Lu–Hf isotopic compositions of the metamorphic gabbro (TW5546-2) in Zeluo, Eastern Tibet, China

Sample Spots	$^{176}Hf/^{177}Hf$	1σ	$^{176}Lu/^{177}Hf$	1σ	$^{176}Yb/^{177}Hf$	1σ	Age (Ma)	$^{176}Hf/^{177}Hf$ (t)	$\varepsilon_{Hf}(t)$	1σ	T_{DM1}	$f_{Lu/Hf}$
TW5446-2-01	0.282690	0.000022	0.002940	0.000024	0.101114	0.001100	438	0.282666	5.9	1.0	840	-0.91
TW5446-2-02	0.282732	0.000016	0.002387	0.000049	0.082513	0.001645	435	0.282713	7.5	0.8	765	-0.93
TW5446-2-03	0.282697	0.000017	0.002564	0.000021	0.086965	0.000645	428	0.282676	6.0	0.8	820	-0.92
TW5446-2-04	0.282717	0.000016	0.002289	0.000040	0.079411	0.001298	441	0.282698	7.1	0.8	785	-0.93
TW5446-2-05	0.282703	0.000016	0.002303	0.000033	0.078409	0.001008	442	0.282684	6.6	0.8	805	-0.93
TW5446-2-06	0.282687	0.000016	0.002530	0.000035	0.090051	0.001407	411	0.282668	5.3	0.8	834	-0.92
TW5446-2-07	0.282709	0.000021	0.002312	0.000027	0.080026	0.001046	441	0.282690	6.8	0.9	796	-0.93
TW5446-2-08	0.282722	0.000020	0.002571	0.000034	0.088393	0.001489	434	0.282701	7.0	0.9	784	-0.92
TW5446-2-09	0.282696	0.000017	0.002377	0.000016	0.080784	0.000676	439	0.282676	6.3	0.8	818	-0.93
TW5446-2-10	0.282702	0.000020	0.002685	0.000013	0.090793	0.000374	433	0.282681	6.3	0.9	815	-0.92
TW5446-2-11	0.282679	0.000018	0.003034	0.000084	0.101250	0.003135	445	0.282654	5.6	0.9	858	-0.91
TW5446-2-12	0.282717	0.000015	0.001908	0.000053	0.064589	0.001933	438	0.282702	7.1	0.8	776	-0.94
TW5446-2-13	0.282688	0.000016	0.002066	0.000022	0.071098	0.000638	433	0.282671	5.9	0.8	823	-0.94
TW5446-2-14	0.282704	0.000017	0.002533	0.000028	0.088888	0.001334	438	0.282683	6.5	0.8	809	-0.92
TW5446-2-15	0.282760	0.000017	0.002640	0.000016	0.089435	0.000723	441	0.282738	8.5	0.8	729	-0.92
TW5446-2-16	0.282707	0.000017	0.002137	0.000051	0.074404	0.001997	463	0.282688	7.2	0.8	796	-0.94
TW5446-2-17	0.282693	0.000015	0.002744	0.000029	0.094042	0.000919	438	0.282671	6.1	0.8	830	-0.92
TW5446-2-18	0.282727	0.000015	0.001556	0.000031	0.048930	0.001346	436	0.282714	7.5	0.8	755	-0.95
TW5446-2-19	0.282720	0.000015	0.002193	0.000055	0.075176	0.002085	442	0.282702	7.2	0.8	778	-0.93
TW5446-2-20	0.282684	0.000017	0.003067	0.000015	0.104438	0.000740	425	0.282659	5.4	0.8	852	-0.91
TW5446-2-21	0.282688	0.000017	0.002006	0.000025	0.067680	0.000659	441	0.282671	6.1	0.8	821	-0.94
TW5446-2-22	0.282697	0.000017	0.002402	0.000031	0.082690	0.001009	445	0.282677	6.4	0.8	817	-0.93
TW5446-2-23	0.282707	0.000016	0.001958	0.000023	0.067541	0.000864	443	0.282691	6.9	0.8	792	-0.94
TW5446-2-24	0.282722	0.000015	0.002440	0.000057	0.083369	0.001832	438	0.282701	7.2	0.8	781	-0.93
TW5446-2-25	0.282726	0.000017	0.002398	0.000051	0.081705	0.001874	428	0.282707	7.1	0.8	774	-0.93